JOURNAL OF GEOPHYSICAL RESEARCH, VOL. 106, NO. 2, PAGES 3237–3260, FEBRUARY 25, 2001

Constraints on magnitudes of extension on Venus from slope measurements

Chris Connors[1] and John Suppe

Department of Geological and Geophysical Sciences, Princeton University, Princeton, New Jersey

Abstract. Slopes related to normal fault scarps on Venus appear in Magellan synthetic aperture radar (SAR) images as tonal bands of increased or decreased radar backscatter relative to adjacent regions. Calculations, through measurements on Magellan stereo SAR, of 170 of these surfaces in plains regions show that their mean topographic slope is 36.4° ± 1.2°, regardless of height. Because there is little to no erosion on Venus, we infer from this mean slope that most faults have collapsed to talus slopes, approximately at an angle of repose, and thus the effective cohesive strength of the crust near most fault surfaces is low, probably because of secondary faulting and jointing. In areas well imaged by Magellan stereo SAR we show that simple, balanced cross sections through individual grabens on Venus can be made, assuming a Coulomb shear angle for fault orientation, thus constraining slip on causitive faults and extension across the grabens. In rifted areas imaged by one Magellan SAR viewing geometry, constraints on extension across rift zones can be made by measuring the tonal bands representing slopes related to individual normal faults and using the mean topographic slope calculated for similar slopes imaged in stereo SAR. With this technique we show that crustal extension due to faulting and folding for the most recent deformation in the Beta rift zone is <20 km. These modest strains, across one of the best developed rift zones on Venus, put severe limits on tectonic models of Venus that invoke significant lateral displacements of the Venusian crust.

1. Introduction

Terrestrial synthetic aperture radar (SAR) and side-looking airborne radar (SLAR) are powerful remote-sensing tools for structural analyses on Earth. In regions of high cloud cover, dense vegetation, and poor access, SAR images are often the most informative data available [*Sabins*, 1987; *Drury*, 1987]. Similarly, SAR is able to penetrate the dense atmosphere of Venus, which highly scatters visible light. Data from radar missions to Venus have become the most useful data for structural interpretations of Venus because they provide the highest-resolution images of the surface of the planet.

The first tectonic features identified on Venus were based on interpretations of Pioneer Venus SAR images [*Masursky et al.*, 1980], which had an ~30 km resolution [*Sanders et al.*, 1991]. Interpretations of the morphology of the imaged highland regions included the inference of rifting on Venus, similar to continental rifting on Earth [*Schaber*, 1982; *McGill et al.*, 1983; *Campbell et al.*, 1983]. Venera 15/16 synthetic aperture radar (SAR), which had a 1–2 km resolution [*Barsukov et al.*, 1986], imaged many previously unknown tectonic features, including the spectacular ridge belts of the northern hemisphere plains from 120° to 250° [*Basilevsky et al.*, 1986; *Frank and Head*, 1990]. In addition, the mountain belts around Lakshmi Planum were imaged at large enough incidence angles to highlight topographic slopes [*Crumpler et al.*, 1986], whereas analyses of Magellan SAR, with a 120–280 m range resolution [*Pettengill et al.*, 1991], have led to identification of many previously unknown map-scale compressive and extensional features, including detailed features that appear to be individual fold limbs and associated fault scarps (e.g., Figures 1 and 2) [*Solomon et al.*, 1992; *Squyres et al.*, 1992; *Suppe and Connors*, 1992]. Although some estimates of strain across structures have been made in the plains regions [e.g., *Bilotti*, 1997] and tessera [*Ghent and Hansen*, 1999], significantly, quantification of strain, such as extension due to slip on individual normal faults, has not been achieved.

One of the principal limitations to quantification of surface deformation on Venus is the lack of high-resolution topography. The highest-quality, global topographic data for Venus are Magellan altimetry, which generally have >10 km horizontal resolution [*Pettengill et al.*, 1991; *Ford and Pettengill*, 1992]. Although Magellan SAR has significantly higher spatial resolution, topography can only be inferred from a single SAR image because there is an inherent topographic ambiguity in a single SAR image. For example, the width of a tonal band representing a discretely dipping surface in a SAR image is a function of both the height and slope of the surface. Thus with one SAR image we can often ascertain that a surface is dipping relative to adjacent flat-lying areas (because of the band of distinct backscatter; see Figure 3), but we cannot know to what extent the width of the band is due the height of the surface versus the slope of the surface. Approximately 20% of the planet was imaged at different radar viewing geometries, allowing a stereoscopic view of these areas. With these stereo images, quantification of surface morphologies is possible in many cases [*Leberl et al.*, 1992; *Connors*, 1995]. In this report we focus on quantifying the surface shape of slopes related to normal faulting using Magellan stereo SAR in order to constrain extensional strain on Venus. We first present a method-

[1]Now at Department of Geology, Washington and Lee University, Lexington, Virginia.

Paper number 2000JE001256.
0148-0227/01/2000JE001256$09.00

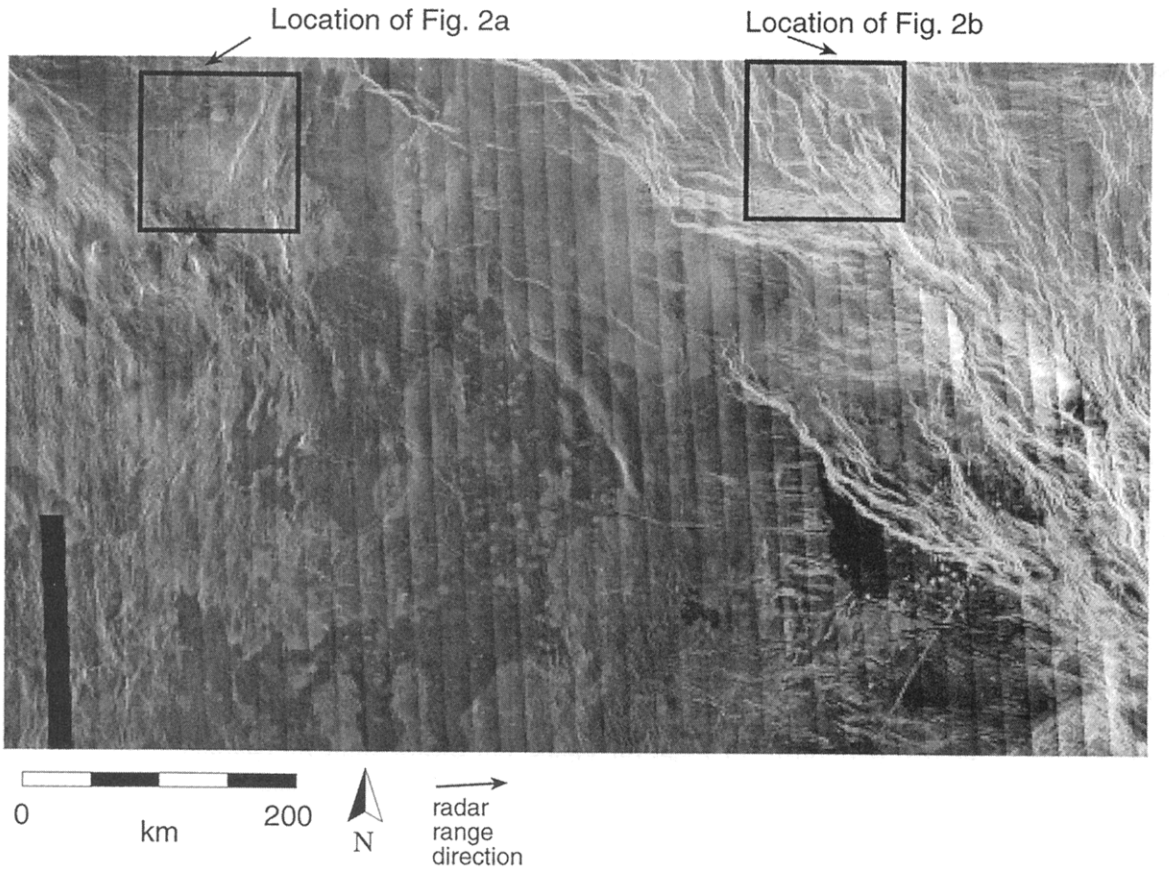

Figure 1. Examples of structural features in Magellan cycle 1 synthetic aperture radar (SAR) image located at about 18°N, 180°; cycle 1 incidence angle $\Omega' \approx 45°$. At this scale, discretely dipping surfaces related to tectonic processes appear as bright and dark lines, and it is difficult to determine whether structures are compressive or extensional.

ology for structural interpretations of Magellan SAR, then give a detailed example of a well-imaged graben. Finally, in a more general way, we make first-order estimates of extension magnitude across Devana Chasma in Beta Regio, one of the great rift zones on Venus.

2. Structural Interpretations of Magellan SAR

Venus is a planet whose surface has undergone little large-scale erosion [*Arvidson et al.*, 1992]. Thus on Venus the planet's surface in a deformed region is essentially the deformed shape, whereas the surface of the Earth in a deformed region is an eroded shape, even in the most arid environment. Therefore one can constrain deformation from surface shape on Venus but not generally on Earth. Thus SAR data that indicate the topography of a feature can be used to determine the geometry of structures on Venus but not on Earth. The distinct bright and dark bands in Figures 1 and 2 are due to discretely dipping surfaces on the surface of Venus of significantly higher topographic slope than adjacent flat-lying regions. The overwhelming majority of such features are clearly related to deformation of the Venusian crust. Except for the occasional lava channel [*Baker et al.*, 1992], no other process is known, in the absence of erosion, that causes these abundant linear features. However, topographic contours of the Venusian surface are not necessarily directly equivalent to structure contours. For example, down-slope movement of a brecciated fault surface may lead to a topographic slope that is closer to angle of repose than to the original fault plane dip. Nonetheless, the geomorphology of deformed areas on Venus closely reflects underlying structural geometries, and therefore qualitative and semi-quantitative analyses of structures on Venus can be carried out in the absence of stratigraphic or subsurface information.

2.1. Distinguishing Between Extensional and Compressive Structures

When interpreting Magellan SAR, one can identify discrete slopes by recognizing differences in radar backscatter from adjacent areas of lower or higher topographic slope. Consider the trough in Figure 3 striking parallel to the path of the satellite (along track direction). Assuming constant surface roughness and dielectric constant across the trough, the west facing surface of this trough (the slope on the right that faces to the left in Figure 3) will display higher backscatter in left-looking cycle 1 and 3 Magellan SAR images because this slope faces toward the antenna and thus scatters more energy in the direction of the antenna. This higher backscatter will generally appear distinctly more radar bright than nearby flat areas in the images. Likewise, the east facing surface will have lower backscatter (will appear dark in radar images) because it faces away from the antenna and thus scatters most of the energy away from the antenna. Therefore, in the right-looking cycle 2 image the brightness of the faces will be reversed. Cycle 1 and 3 SAR images are said to be "left-looking" because the an-

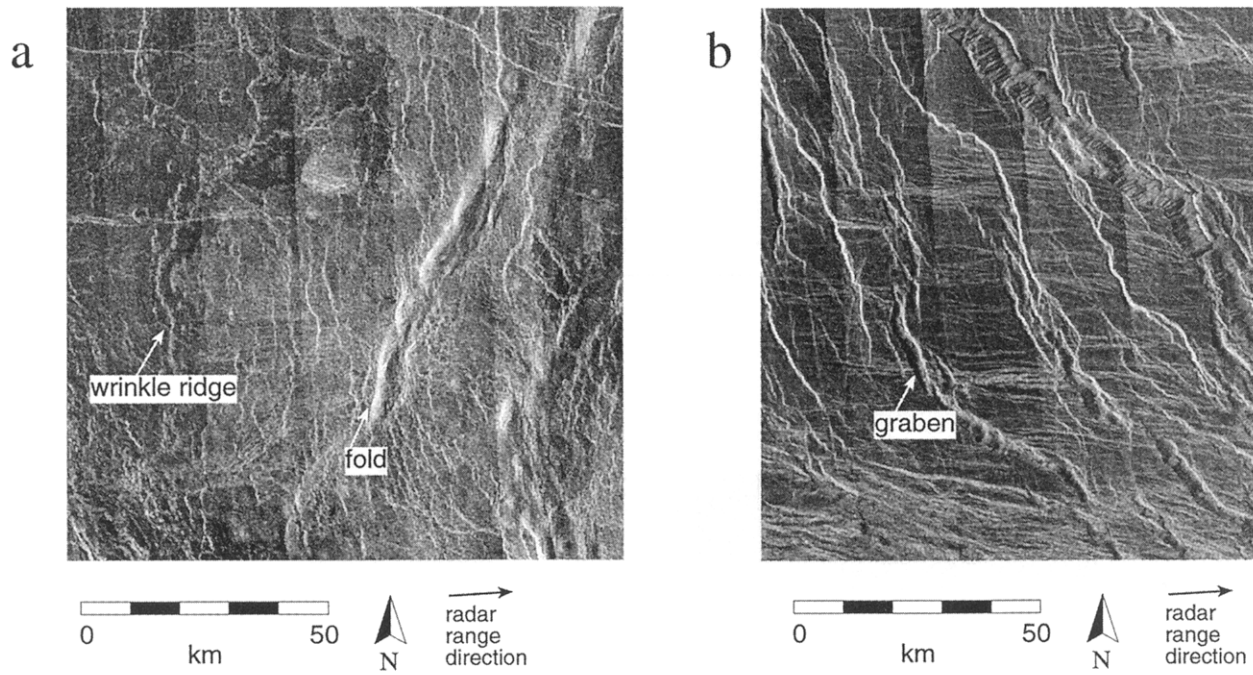

Figure 2. Enlargement of selected regions from Figure 1 showing compressive and extensional structures in Magellan cycle 1 SAR images located at about 18°N, 180°; $\Omega' \approx 45°$. (a) Deformed volcanic plains displaying through-going, positive-relief features with gradual changes in radar backscatter on sides of structures. These attributes are consistent with an interpretation of compressive deformation. Also displayed are irregular, low-relief bright features, known as wrinkle ridges. These are interpreted as being compressive on the basis of their similarity to wrinkle ridges analyzed on other terrestrial planets. (b) Deformational features in volcanic plains recognizable as through-going features that have negative-relief relative to undeformed plains. Additionally, the transition in radar backscatter is discrete and abrupt from undeformed plains. These observations are consistent with deformation of the plains in this area by extensional processes.

tenna transmitted and received microwave energy to the left of the imaged surface; cycle 2 images are "right-looking" because the antenna was to the right of the image in this cycle. Thus, if the trough of Figure 3 is a tectonic feature, it may be a graben related to extension with normal faults dipping toward the interior of the trough or it may be a compressive syncline with the east and west faces constituting limbs of a fold.

We use the term "graben" quite liberally here; the bounding surfaces could very likely be a normal fault and a related extensional fold limb. In addition, as we discuss in detail later, we believe that the actual imaged surfaces related to normal faulting are usually not primary fault scarps, but have collapsed to talus slopes. For simplicity, we use "graben" here to imply that a trough is extensional, though not tensile, in origin.

The most useful criterion for distinguishing individual map-scale compressive folds from graben in Magellan SAR is the along-strike termination of the west and east faces of the feature. If both sides of the negative-relief feature in Figure 3 terminate at the same position along strike (Figure 2b), then the feature is more plausibly a graben because the genetically related features of the extensional structure are the two bounding normal faults. If the bright (right) and dark (left) faces of the trough terminate at different points along strike, that is, if the trough is bounded by two positive relief ridges, then the trough is more likely a syncline between two different compressive folds. The genetically related front and back limbs of a compressive anticline will more likely terminate at the same position along strike where they define one positive-relief feature. Figure 2 shows an example of both compressive and extensional features deforming volcanic plains. Note that analysis of higher-resolution images is necessary in many places in order to make this distinction (compare Figure 1 with Figure 2). It should be noted that determining the along-strike character of features can be very difficult in areas that are deformed by multiple folds and faults so that recognition of individual features may be impossible. In these cases the edges of deformation zones often provide insight into the style of deformation in the more deformed interiors (Figure 4).

The discreteness in which a slope appears relative to adjacent flat-lying areas in Magellan images provides additional information for determining its structural origin. Scarps related to normal faulting are generally more sharply defined than axial surfaces associated with compressive folds in Magellan images (e.g., Figure 2). This is because the change in slope is usually much greater for fault scarps (even if the scarp has later collapsed to a talus slope) than for fold limbs, and thus the radar images scarps more distinctly. Although this report will not look in detail at topographic slopes related to contractional structures, measurements we have made indicate that such slopes generally fall in the range of 10°–15°. We quantify the range of slopes related to normal faulting in section 4, and we show that these slopes are considerably higher than those related to compressive structures, on average.

It is tempting to conclude that for surfaces facing the antenna, higher backscatter indicates steeper slopes. For example, the slopes related to normal faulting in Figure 2b do appear brighter than the slopes related to the compressive folds in Figure 2a. This is in fact often the case, but caution

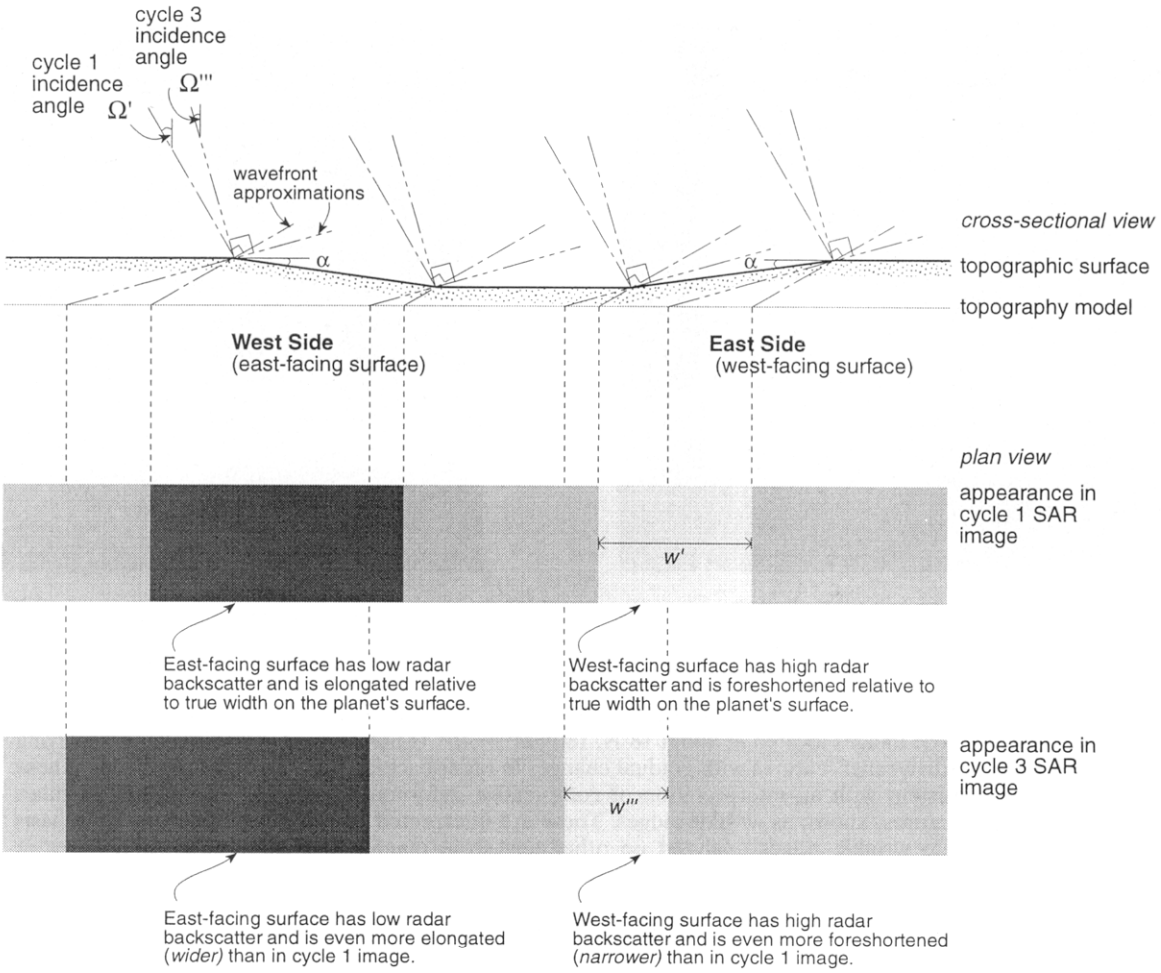

Figure 3. Shown are the expected ground range in left-looking cycle 1 and cycle 3 Magellan SAR images of a symmetric topographic trough striking parallel to the azimuth direction (the direction the antenna is moving as SAR is collected). The west facing surfaces display higher radar backscatter because more energy is returned to the antenna than in the flat-lying areas around the trough, while the east facing surfaces display lower backscatter. Projection of radar wave fronts from the surface to the topography model determines the position of a feature in a SAR image. Thus dipping surfaces are distorted relative to their true width and position. Because of these radar distortions, the appearance of the trough is not symmetric.

must be exercised in this regard because steep slopes that are laid over (surfaces where the crest is imaged before the base) can have a ghostly appearance that is not significantly high in backscatter (Figure 5a). We discuss layover in more detail below. In addition, when one is attempting to compare different slopes, rather than a slope with an adjacent flat-lying area, the assumption of constant surface roughness is not valid. Thus one would have to independently know the surface roughness of both slopes and their adjacent flat-lying areas to be confident in concluding that the higher backscatter indicated a steeper slope.

The sinuosity of the strike of a surface related to tectonic processes can also provide insight into the surface's origin. Bands of high or low backscatter related to normal faulting often appear straight along strike on Venus, or if not straight they form en echelon segments. On the other hand, thrust faults and their associated folds are generally, but not always, discontinuous and irregular. The best examples of this irregular strike are the ubiquitous wrinkle ridges of Venus [*Bilotti and Suppe*, 1992] (Figures 2a and 5). Some of these features appear to be positive-relief features with low or irregular changes in backscatter of the surfaces, but primarily they are interpreted to be contractional because of their similarity to wrinkle ridges analyzed on other terrestrial planets [*Plescia and Golombek*, 1986; *Watters*, 1988; *Golombek et al.*, 1991]. This contrast of the discontinuous and irregular character of thrust faults and related folds versus the long, straight character of normal faults on Venus is perhaps expected on a planet devoid of significant erosion. If most of the Venusian upper crust is produced by volcanism [*Head et al.*, 1992], then there is probably much more significant vertical, as opposed to horizontal, mechanical anisotropy in the upper crust. This is because each lava flow will be much more similar to itself than to other lava flows above and below it. In addition, the exposed surface of a given flow may constitute a weathered zone so that the tops of older flows may have a different strength than the rest of the flow below it or a subsequent flow above it. Lateral propagation of subhorizontal thrust faults should thus be more discontinuous than should lateral propagation of more steeply dipping normal faults, which cut through the volcanic strata. In addition, most isolated thrust faults on Earth dip more shallowly than isolated normal faults [*Suppe*, 1985]. Thus minor

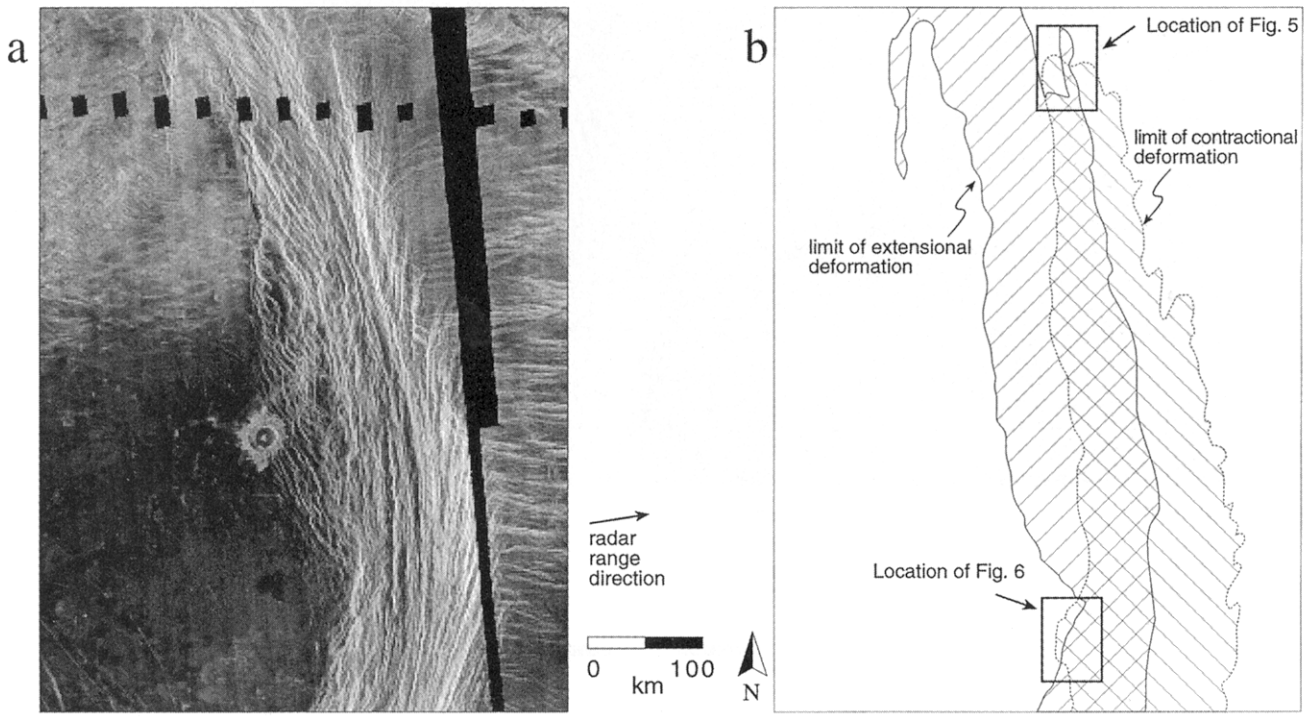

Figure 4. (a) Magellan cycle 1 SAR image of the northeastern portion of the deformation belt known as Artemis Chasma at about 30°S, 140°; $\Omega' \approx 34°$–$33°$. Superposed deformation is common in this belt (see Figures 5 and 6). (b) Shown are regions within the belt intrepreted to have experienced contractional and extensional deformation on the basis of the criteria described in the text. Lesser deformational features of a different generation exist outside the belt in different orientations. The belt is sufficiently deformed that analysis of the interior alone probably would not allow determination of tectonic style, but by analyzing the edges of the deformation zone, one can infer interior deformation.

changes along strike in the dip of a low-angle thrust fault will have a much greater effect on the sinuosity of the strike than will minor changes along strike in the dip of a high-angle normal fault.

These criteria, although not always unambiguous, are extremely useful and are demonstrated for both extensional and compressive structures in the images in Figures 4–6. In this complicated deformation belt known as Artemis Chasma are displayed both graben and compressive folds with overprinted structures from multiple deformational episodes (Figure 4). We show the regions that we interpret as having experienced extensional, compressive, or both types of deformation.

2.2. Quantifying Slopes and Heights of Surfaces

Qualitatively inferring the topographic relief of a feature by recognizing distinct bands of radar backscatter in a SAR image is probably obvious to most interpreters of Magellan data, and most structural interpretations of tectonic features on Venus seem to be based on criteria similar to those discussed above [e.g., *Solomon et al.*, 1992; *Squyres et al.*, 1992; *Suppe and Connors*, 1992]. However, the positions of these distinct bands of radar backscatter in the images are not intuitive and are not taken into consideration in most interpretations of Magellan SAR. For analyses of large areas this is permissible because the distortions in the positions of features in SAR are not readily apparent in regional images such as Figures 1 and 4. But these distortions are very apparent in detailed views, and for accurate analyses of individual structures, including any attempt at quantifying deformation, one must properly consider these distortions. For example, Figure 5a shows images with three different radar imaging geometries covering the same region of the surface of Venus. Discrete bands of radar backscatter are recognizable in all three images, but the width, character, and position of the bands change dramatically between the three images. A complete explanation of radar distortions is beyond the scope of this report, but because we make use of them throughout this analysis, we present a brief description below. A more detailed description is given by *Moore* [1983] and *Leberl* [1990]. A Magellan-specific treatment with emphasis on slopes is given by *Connors* [1995].

SAR images are constructed by mapping the radar wave front onto a low-resolution topography model (Figure 3). The height of the topography model used in the processing of most Magellan SAR is based primarily on Pioneer Venus altimetry. These values vary over large distances, but because the resolution of the topography model is >26 km/pixel, the topography model approximates a plane at the scale of the structures we are concerned with in this report. Therefore knowledge of the elevations of the topography model is not necessary for relative height and slope determinations. Exact elevations of the topography model are required only for absolute elevation determinations. Thus for the local slopes analyzed in this report we can approximate the topography model with a horizontal plane in the region of interest.

One additional point regarding the topographic model needs to be kept in mind. The stereoscopic impression of an image pair depends on differences in the positions of features

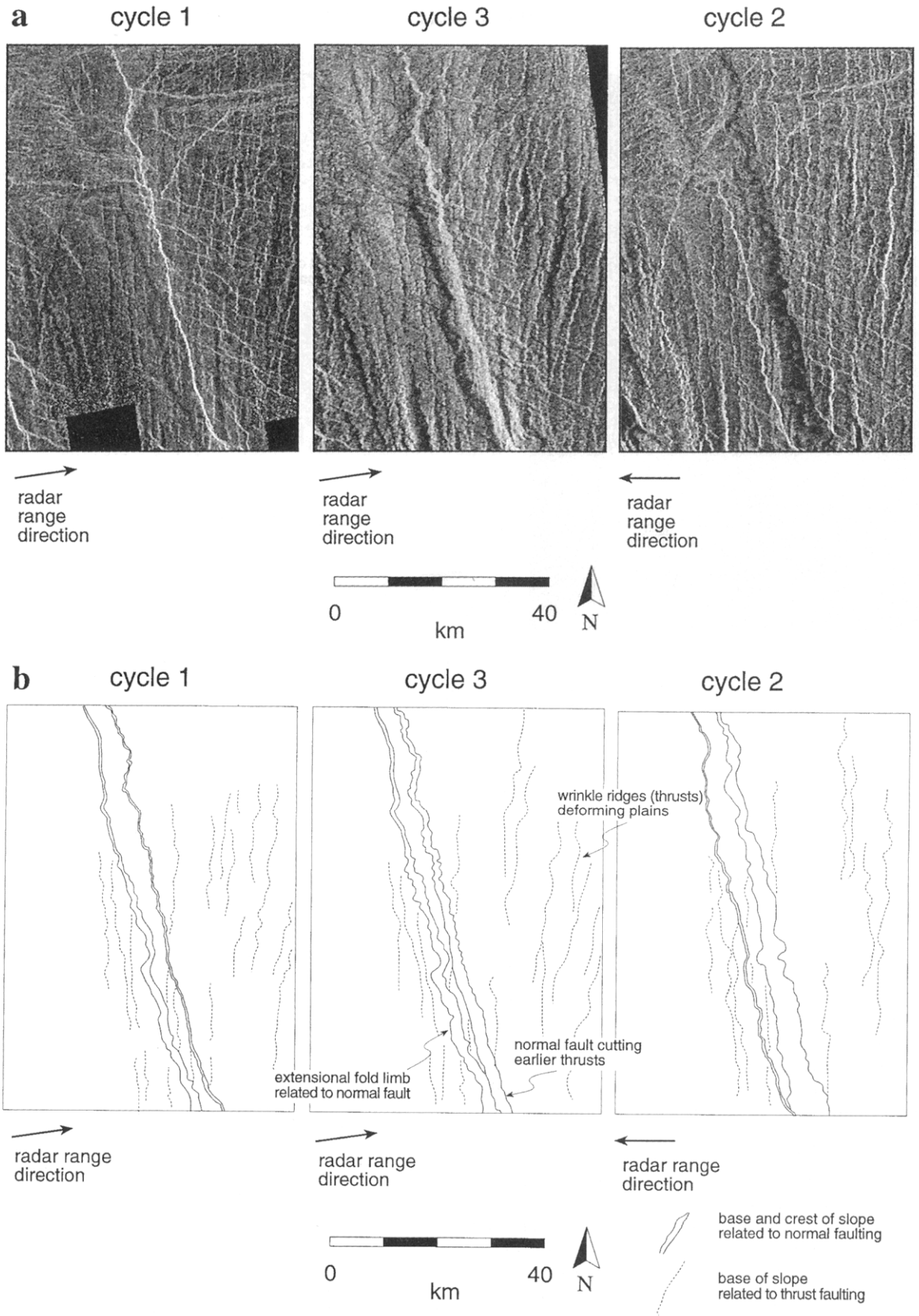

Figure 5. (a) Region within Artemis Chasma deformation belt shown in three different Magellan SAR images from three different imaging cycles (see Figure 4 for location); $\Omega' \approx 34°$, $\Omega''' \approx 18°$, $\Omega'' \approx 25°$. The area shows extensional overprinting of graben cutting contractional wrinkle ridges (thrusts). The images demonstrate the dramatic changes in the appearance of a surface when the radar imaging geometry is changed. The east side of the graben has a topographic slope of ~42°, which is larger than the radar incidence angle for both the cycle 1 and 3 images. Thus the slope is laid over in both images; that is, the crest of the surface is imaged to the left of the base of the surface (see Figure 7). This surface will not stereoscopically fuse, but regions around the surface may (compare with Figure 6a, in which the imaged slope will fuse). (b) Interpretation of structural features from three SAR images shown in Figure 5a.

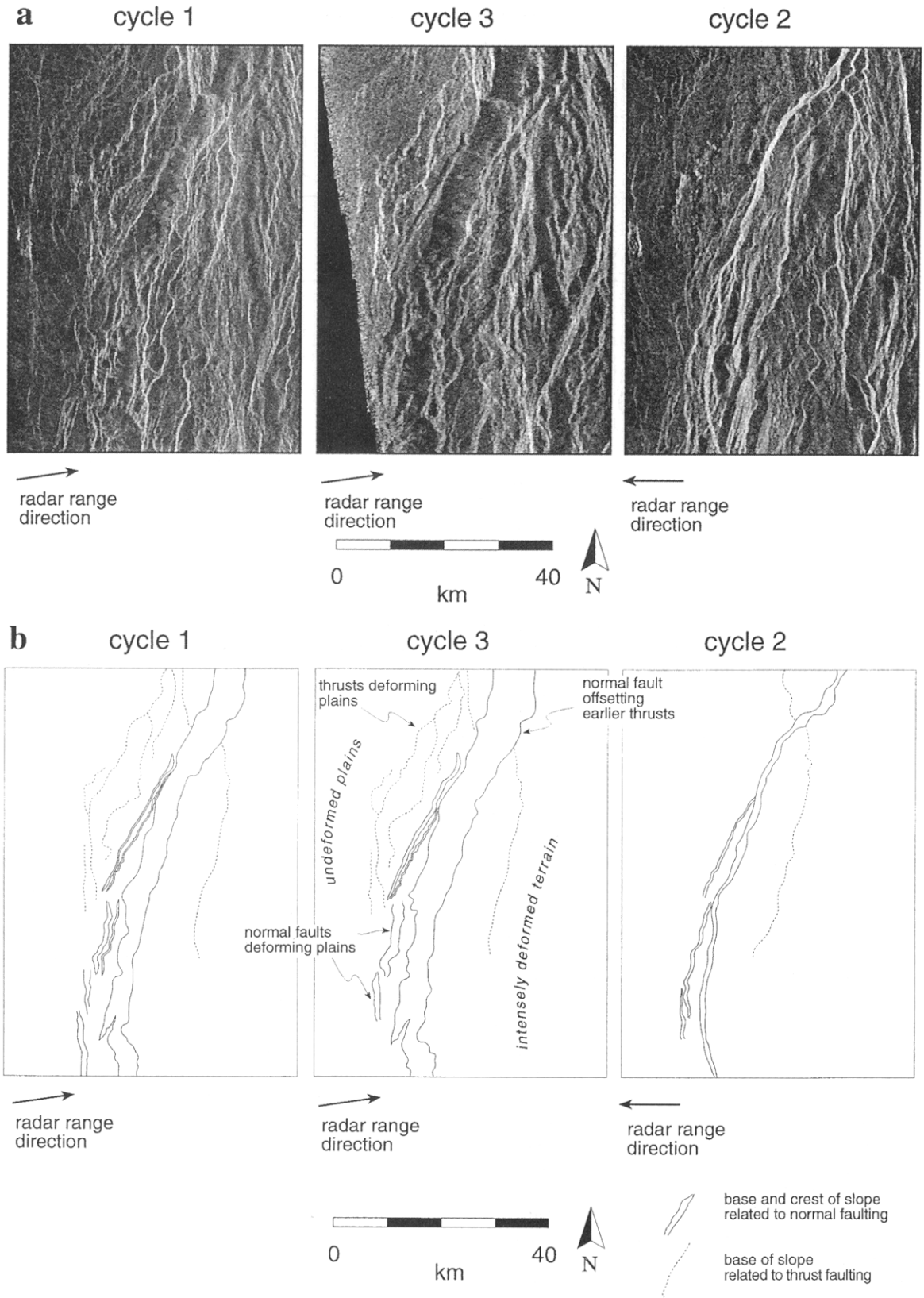

Figure 6. (a) Region within Artemis Chasma deformation belt shown in three different Magellan SAR images from three different imaging cycles (see Figure 4 for location); $\Omega' \approx 33°$, $\Omega''' \approx 17°$, $\Omega'' \approx 25°$. As in Figure 5, extensional structures cut older contractional structures as well as previously undeformed plains. The major NNE striking surface is related to a normal fault that cuts imbricated thrusts, showing west-to-east offset in north-south trending thrusts. The west side of the surface has a topographic slope of ~32° and is interpreted to represent collapse of the fault to a tallus slope. Because the main surface is facing to the east, the slope is imaged more clearly than the main slope in Figure 5a. Although the surface is elongated relative to its true width, this distortion is perhaps more understandable to most interpreters than imaging of the surface discussed in Figure 5. For example, the surface here will stereoscopically fuse, whereas that in Figure 5 will not. (b) Interpretation of structural features from three SAR images shown in Figure 6a.

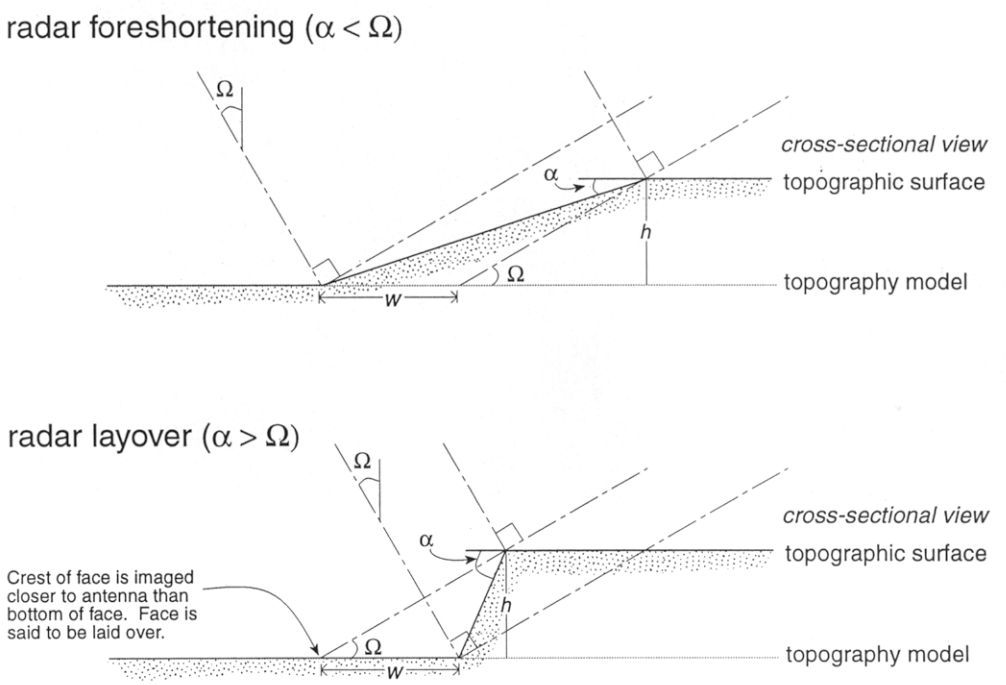

Figure 7. Relationship between the topographic slope α, height h, and width w of a face as seen in left-looking SAR images with an incidence angle Ω; see (1)–(4) for relations. Shown are two faces that have the same height and imaged width but different slopes. (a) Radar foreshortening, a face that is facing toward the antenna, is narrower in a SAR image than its true width on the planet's surface. (b) In radar layover, for a face that is facing toward the antenna, the crest of the face is imaged closer to the antenna than the base of the face. The face may be narrower or wider in the image than the true width.

between images with different radar imaging geometries. Thus the individual surfaces we are concerned with here may be distinguishable in a stereogram, but any broad topographic trends present in the topography model will not be noticeable stereoscopically. This is because both images are mapped to the same topography model, and thus any broad topographic trends are shared by both images. Figure 6a illustrates this phenomenon. The large-scale topographic trend in this area slopes down to the right, but because this trend is incorporated into the low-resolution topography model during processing of the images, one does not get the impression of a broad, regional slope to the right when stereoscopically fusing cycle 1 and 3 images. Instead, the image appears relatively flat in stereo. Small-scale features do, however, give a strong stereoscopic impression. For example, the NNE trending scarp appears as a dipping slope to the right because the topographic change associated with this individual surface was not present in the topography model. This is an example of why care must be taken when interpreting stereo radar images, especially for interpreters familiar with stereo aerial photography, because stereo radar differ from these data in fundamental ways.

The projection of the radar wave front onto the topographic model used in the processing of the images determines the positions of features in the Magellan SAR image (Figures 3, 7, and 8). For different radar imaging geometries (incidence angles), a feature of a given height will map to different positions in the different images. These changes in position are radar parallaxes and must be quantified in order to reconstruct the true shape of the slope of interest. The changes in position of features in the images are a function of the orientation of side-looking radar and are described by the nominal incidence angle of the radar. The term "nominal incidence angle" is the angle between the radar beam and the normal to the topography model. We will use simply "incidence angle" in the rest of this paper to refer to this angle. In Magellan SAR the incidence angle changes with latitude and for each cycle; thus the parallax of a feature with a given height will also change between Magellan images from different latitudes or different cycles.

A discretely dipping surface imaged in SAR will be distorted relative to its true position and width on the surface of the planet (see Figure 5a). Note in the bottom of Figure 3 that the surface facing toward the antenna (a west facing surface in cycle 1 and 3 Magellan SAR) is foreshortened relative to its true width and, similarly, the surface facing away from the antenna (the east facing surface) is elongated. For surfaces imaged by Magellan SAR (Figure 7) the relationship between the width of a surface in the image, w, the slope α, the height of a surface, h, and the incidence angle Ω of the radar is given by

$$w = \frac{h(\tan \Omega \pm \tan \alpha)}{\tan \Omega \tan \alpha}. \quad (1)$$

The sign in (1) is positive for east facing surfaces and negative for west facing surfaces. For surfaces in radar shadow (not imaged at all by the radar) a different relation holds. Because we have detected very few cases of radar shadow in Magellan SAR, we will not discuss it further here; a solution is given by *Connors* [1995].

Because there are two unknowns in (1), we cannot determine the height or slope of a face from one SAR image. This demonstrates the inherent topographic ambiguity of a single

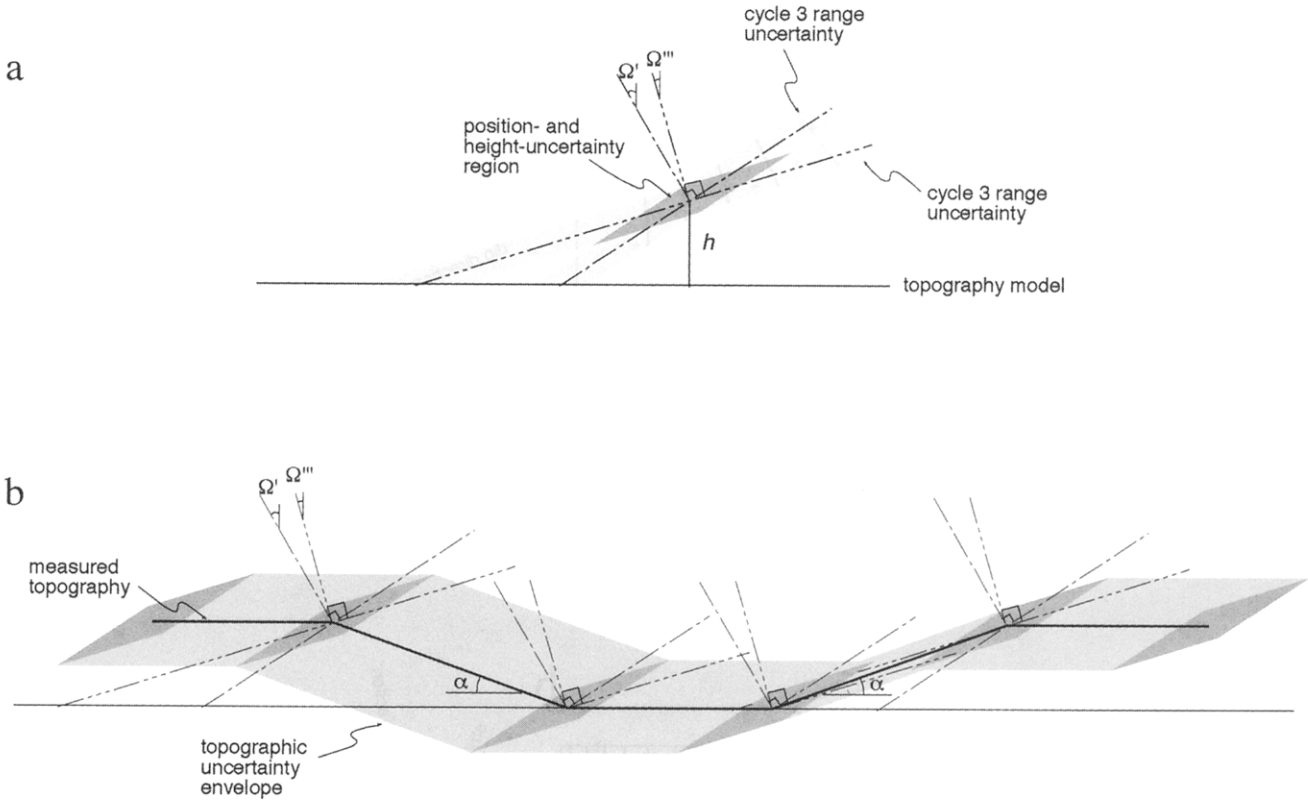

Figure 8. (a) Intersection of two wave fronts with corresponding range uncertainty results in diamond-shaped region of position and height uncertainty [after *Leberl et al.*, 1992]. (b) Topographic uncertainty envelope across a topographic trough. The uncertainty envelope is based on sweeping the diamond-shaped uncertainty region through known heights along trough, such as the crest and base of discretely dipping surfaces. Surfaces facing away from the radar antenna, such as east facing surfaces in cycle 1 and 3 Magellan SAR, will have significantly higher topographic slope uncertainties than west facing surfaces, as can be seen by the wider region of uncertainty for the face on the left side relative to that on the right.

SAR image. For a surface facing away from the antenna, an additional image with a different incidence angle will allow for unique determination of the slope and height of the face, assuming the face is not in radar shadow. Approximately 20% of the planet was imaged at a different incidence angle during cycle 3 mapping. To determine the slope of the face using two images, we take the ratio of (1) for the widths measured in both cycle 1 and 3 images:

$$\frac{w'''}{w'} = \frac{\tan \Omega'(\tan \Omega''' \pm \tan \alpha)}{\tan \Omega'''(\tan \Omega' \pm \tan \alpha)}, \tag{2}$$

where one tick mark refers to parameters in cycle 1 images and three ticks refer to parameters in cycle 3 images. As with (1), the sign in (2) is positive for east facing surfaces and negative for west facing surfaces.

The situation is slightly more complicated in the case of surfaces facing toward the antenna because the crest of a surface may be imaged before the base (Figure 7b), in which case the relative positions of the surface are reversed from their true positions on the surface of the planet. This situation is known as radar layover and is common in Magellan SAR, particularly cycle 3 images, because of the small incidence angles used and because there are many large, relatively steep slopes on Venus. Solutions using (1) and (2) are valid for laid over slopes where w is negative, but because one does not know a priori whether a face is foreshortened or laid over, measurements from two images with different incidence angles such as cycle 1 and 3 Magellan SAR will still not uniquely determine the shape of the surface. This is because there will still be two valid slope and height combinations using (2) for west facing surfaces. Additional information such as cycle 2 images, Magellan altimetric echoes, or inferences from the stereoscopic impression of features near the face is needed to uniquely determine the imaging of a west facing surface and thus the slope and height of the face [see *Connors*, 1995].

The slope of the surface in (1) and (2) is measured in the range direction and thus is an apparent slope of the true topographic slope. The apparent slope α is related to the true topographic slope α_{true} by

$$\tan \alpha_{true} = \tan \alpha / \cos \gamma, \tag{3}$$

where γ is the acute angle between the dip direction of the face and the range direction of the radar, or equivalently, the acute angle between the strike of the face and the azimuth direction (Figure 9). The strike of a face and the cycle in which the slope was imaged have a dramatic effect on whether a face is laid over or foreshortened. For example, a face with $\alpha_{true} = 40°$ (to the west) in a cycle 1 image will be foreshortened within the latitude range ~35°N to 15°S. Outside of this range, whether the face will be foreshortened or laid over is highly dependent on the strike of the face relative to the radar range direction, whereas this same face in a cycle 3 image will always be laid

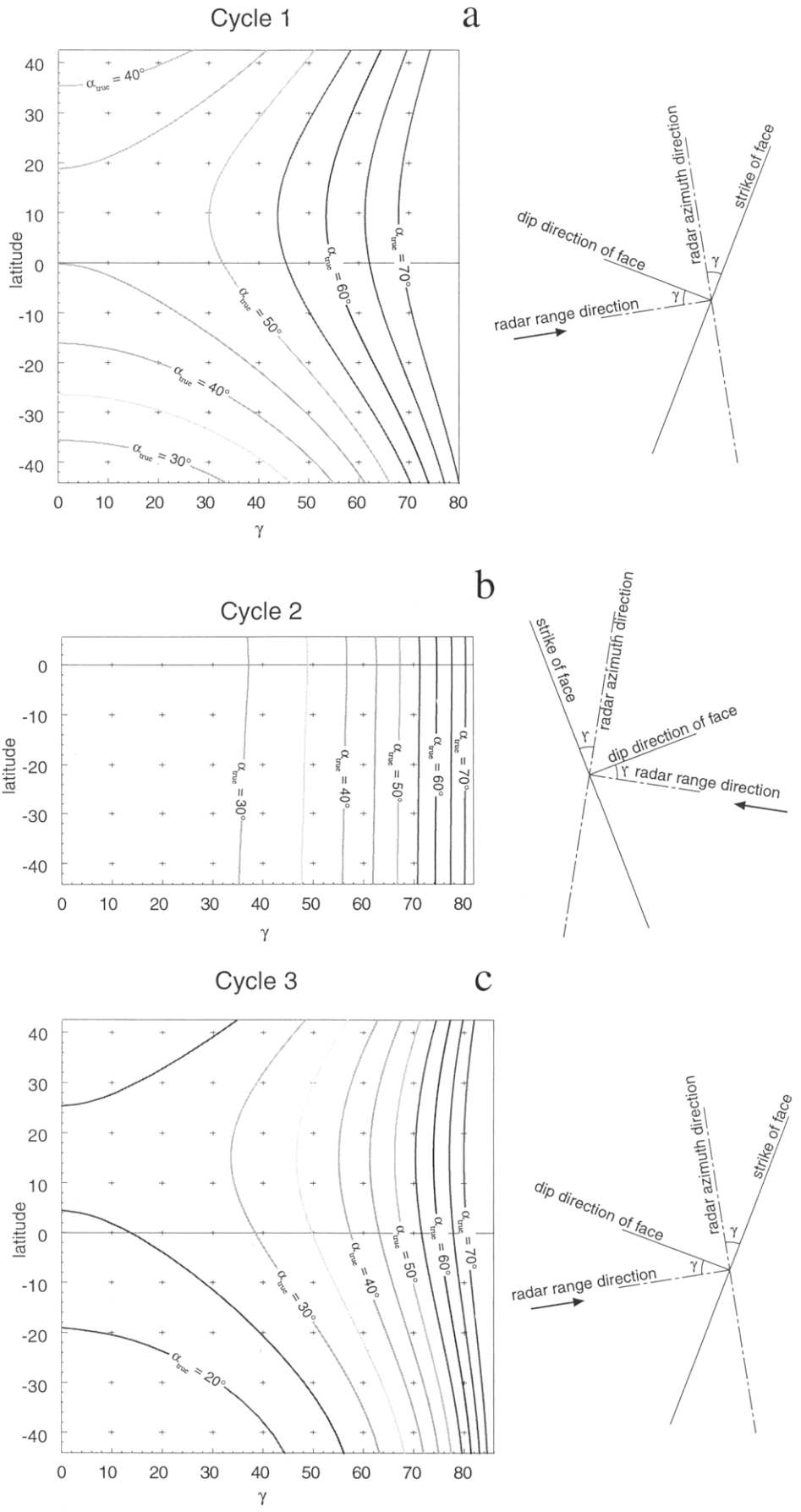
Cycle 1
a
latitude
γ
α_{true} = 40°
α_{true} = 50°
α_{true} = 60°
α_{true} = 70°
α_{true} = 40°
α_{true} = 30°
dip direction of face
radar azimuth direction
strike of face
radar range direction
γ
b
Cycle 2
latitude
γ
α_{true} = 30°
α_{true} = 40°
α_{true} = 50°
α_{true} = 60°
α_{true} = 70°
strike of face
radar azimuth direction
dip direction of face
radar range direction
γ
c
Cycle 3
latitude
γ
α_{true} = 20°
α_{true} = 30°
α_{true} = 40°
α_{true} = 50°
α_{true} = 60°
α_{true} = 70°
dip direction of face
radar azimuth direction
strike of face
radar range direction
γ

over unless the strike of the face is greater than ~55° from the radar range direction (Figure 9). Thus it is often very difficult to recognize equivalent features imaged in different cycles without a strong understanding of the imaging geometry between cycles. Figures 5 and 6 provide vivid examples of the difference in imaging of surfaces between the different cycles.

One can solve for the height h of an object above the topography model through the relation of *Leberl et al.* [1992],

$$h = dp/(\cot \Omega''' - \cot \Omega'), \quad (4)$$

in the case of east facing surfaces, $dp = w''' - w'$, and for west facing surfaces, $dp = w' - w'''$ [*Connors*, 1995]. As with slope determinations, w is negative for laid over slopes. By far, the best imaged slopes in Magellan SAR suitable for quantifying their geometry using these relations are those related to normal faults, and we look more closely at a well-imaged example below.

The potential uncertainty in the position of a feature is a result of the range ambiguity of the radar. Consider the intersection of two wave fronts with corresponding range uncertainties (Figure 8a). The region of uncertainty will be a diamond-shaped region for any one point [*Leberl et al.*, 1992]. Because the orientation of a face is determined by the location of two points, the region of uncertainty for a face can be thought of as the diamond-shaped region swept along the calculated face orientation or as an uncertainty envelope with sides parallel to the face orientation. Thus the maximum possible slope is from the top of the diamond-shaped uncertainty of the point at the crest of the face to the bottom of the diamond-shaped uncertainty of the point at the base of the face (Figure 8b). Using (2), it can be shown that topographic slope uncertainties are dependent on both the orientation and magnitude of the topographic slope [*Connors*, 1995]. For example, for east looking SAR, such as Magellan cycles 1 and 3, east facing surfaces will have significantly higher topographic slope uncertainties than west facing surfaces. Figure 8b provides a more intuitive understanding of this phenomenon. The stereo-intersection angle is defined as the angle between the two incidence angles, $\Omega' - \Omega'''$ [*Leberl et al.*, 1992], or the small angle of the diamond-shaped region of uncertainty. For all imaging geometries this angle will be smaller than its supplement; thus the long axis of the uncertainty diamond will always be closer to perpendicular with surfaces facing away from the radar antenna than with those facing toward the antenna. For surfaces facing toward the antenna, slope uncertainty is smallest when $\alpha = (\Omega''' + \Omega')/2$ and greatest when $\alpha = 90°$. For surfaces facing away from the antenna, slope uncertainty is smallest when $\alpha = 0°$, and greatest when $\alpha = 90° - \Omega'$. Height uncertainties of faces do not share this dependency and are a function only of the incidence angles and range uncertainties of the radar.

2.3. Example

The area shown in Figure 5a lies within the deformation belt shown in Figure 4 known as Artemis Chasma, where two distinct structural elements are found: throughout the image sinuous ridges strike approximately north-south, and in the center of the image a straighter trough strikes about N 14° W. The low-relief, sinuous ridges clearly have positive relief, but their topographic expressions are too subtle to use the techniques described above to quantify their shape. Nonetheless, the sinuous strike and gradual backscatter changes across the positive-relief features are characteristics distinct enough that we have confidence in calling them wrinkle ridges and interpreting them as compressive structures. The trough has faces that have discretely different backscatter from the adjacent areas and appear superposed on the wrinkle ridges. The faces of the trough are relatively straight and lack the sinuosity of the wrinkle ridges. On the basis of the criteria above, these observations suggest that the trough represents a graben which cuts earlier compressive structures. We seek insight into the causative structural elements of this graben. Since we have no subsurface information, probably the most significant constraints on structural interpretations will come from the topographic slopes of the discretely dipping surfaces bounding the graben. These surfaces, unlike the sides of the wrinkle ridges, are well imaged and large enough to be measurable and allow us to quantify the surface expression of the structure.

Along the line of the cross section shown in Figure 10a, we measured the width of the west face (east side), east face (west side), and central floor of the graben and used (2) and (4) to calculate the height and slope of the faces. The west face has a topographic slope of 41.6° + 5.5°/−3.5° and a height of 1240 ± 224 m. The error limits are maximum measurement uncertainties associated with the range resolution of both images [see *Connors*, 1995]. We measured the widths of the elongated, more poorly imaged east facing surface to determine that it has a much gentler topographic slope of 14.5° + 21.8°/−11.6° and smaller height of 309 ± 224 m. The floor of the graben in between the faces is essentially flat-lying with a topographic slope of 1.9° + 4.2°/−3.3° and a relief of 123 ± 224 m. Thus the graben is asymmetric with the block to the east significantly higher. Projection of wave fronts that separate these discrete changes in backscatter allows us to reconstruct the shape of the surface of the structure graphically (Figure 10b). Shown are the intersections of wave fronts from the cycle 1 and 3 images that define the height and position of each discrete change in surface slope and the corresponding uncertainty envelope for the surface shape of the graben.

Magellan altimetry sampled either side of the west facing surface of the graben and provides a potential check of the height determinations from the SAR. The power-versus-time

Figure 9. (opposite) Dependency of strike on imaging character of a surface. Plots show the small angle γ between strike of face and radar azimuth direction at which a surface with a true topographic slope α_{true} changes from being foreshortened (to right of line) to laid over (to left of line) in Magellan images for different latitudes. For example, a face with $\alpha_{true} = 40°$ (to the west) in a cycle 1 image will be foreshortened within the latitude range ~35°N to 15°S (see Figure 9a). Outside of this range, whether the face will be foreshortened or laid over is highly dependent on the strike of the face relative to the radar azimuth direction, whereas this same face in a cycle 3 image will always be laid over unless the strike of the face is greater than ~55° from the radar azimuth direction (see Figure 9c). (a) Latitude versus γ for cycle 1 incidence angles. The plot is relevant for west facing surfaces. (b) Latitude versus γ for cycle 2 incidence angles. The plot is relevant for east facing surfaces. (c) Latitude versus γ for cycle 3 incidence angles. The plot is relevant for west facing surfaces.

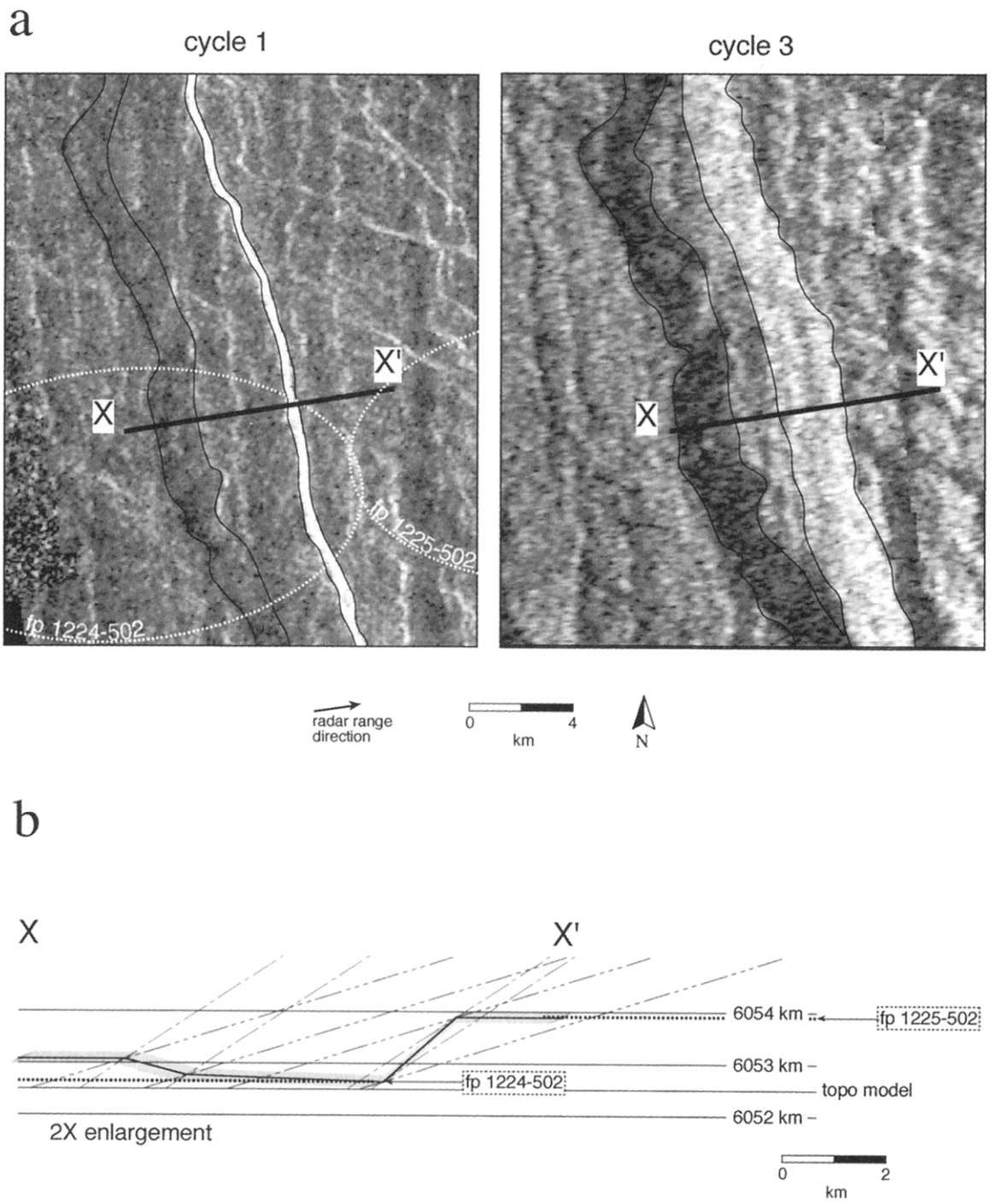

Figure 10. (a) Enlargement of Magellan cycle 1 and 3 SAR images of the graben shown in Figure 5; $\Omega' = 33.5°$, $\Omega''' = 17.5°$. (b) Topographic cross section based on projection of wave fronts onto the topographic model used in processing images (2× enlargement of Figure 10a). Although the sides of the graben appear to be symmetric in the images, the actual topography is very asymmetric. This demonstrates the importance of proper consideration of radar imaging when interpreting structures in Magellan images. Also shown is the uncertainty envelope, in gray, around the topography based on propagation of range resolution uncertainties, see Figure 7, along with comparison with Magellan altimetry where fp 1224-502 refers to altimetry footprint 502 from orbit 1224. See Figure 12 for structural cross sections based on topography.

delay echo of an individual altimetry measurement yields a planetary radius value for the area of strongest radar return within the footprint [*Ford and Pettengill*, 1992]. The footprint of the altimeter is so large that it is often difficult to determine unambiguously where the signal is coming from within a footprint, but in certain select cases it can be used with a single SAR image to ascertain the height and slope of a surface. In this particular instance, it appears that the strongest return to the altimeter is from the base of the graben in footprint 502 of orbit 1224 (labeled fp 1224-502) and the footwall to the east of

the west face in 1225-502, but, of course, we are not getting adequate information on the rest of the structure (Figure 10b). The difference in these radii, 1262 ± 19 m, corresponds closely with our independently derived height of 1240 ± 224 m for the west face from Magellan stereo SAR measurements and suggests that the height and slope uncertainties based on the stereo SAR are conservative. It should be noted that the methods of deriving the uncertainties in the height measurements are quite different. The uncertainty using the width measurements is the maximum possible uncertainty, the envelope of Figure 8, and is always much more conservative than the uncertainty of the fit to the Magellan echoes. *Connors* [1995] discusses the uncertainty estimates in more detail.

3. Constraints on Structural Interpretations

A reasonable structural interpretation of the graben in Figure 10 first requires a consideration of what topographic slopes on Venus related to tectonism may represent in terms of physical processes. Hard rock slopes and related scree slopes can span a wide range of topographic slopes on Earth because of the multitude of processes acting to both create and subsequently modify or maintain their slopes. Besides the inherent strength of the rock mass, probably most significant are water-related processes. Most obvious are stream erosion through hard rock or glacial excavation of valleys, but subsequent undercutting by streams, in combination with jointing, also plays an enormous role in shaping slopes on Earth [*Selby*, 1993]. In addition, groundwater flow and joint orientation are large contributors to hard rock slope stability on Earth [*Terzaghi*, 1962]. In fact, water plays some role in the development of virtually all vertical slopes on Earth. Perhaps counter to intuition, on a planet devoid of water, we would therefore expect to find fewer very steep or vertical slopes than we find on Earth. The discretely dipping surfaces so dramatically apparent in Magellan SAR images of Venus are mostly tectonic slopes formed in the absence of water and thus without these water-related modifications. Therefore topographic slopes and heights of these features are more directly related to underlying structural geometries than on Earth and more directly due to the strength of the rock in which they formed.

Because the surface of Venus is clearly volcanic, probably basalt [*Surkov et al.*, 1983], a rock with high cohesive strength, slopes, such as the graben-bounding faces of Figure 10, may be close to the actual dip of the related faults or fold limbs. However, if the crust near these structures is significantly weakened by secondary faulting and jointing, the imaged surfaces near faults may more closely approximate noncohesive talus slopes with topographic slopes closer to an angle of repose. A decrease in maximum stable slope angles for exposed scarps in Wellington greywacke in New Zealand is observed for slopes close to the Wellington fault and is attributed to the increased fracturing of the rock within 1 km of the fault [*Grant-Taylor*, 1964]. However, because very little erosion has occurred on Venus [*Arvidson et al.*, 1992], we would not expect tectonically related slopes on the Venusian surface to be less than the angle of repose, unless the primary structural dip of the feature was less than the angle of repose, such as a fold limb, or unless subsequent deformation occurred, such as slip on multiple faults.

Let us return to the graben in Figure 10 with the above considerations in mind. In this case, we can rule out subsequent deformation because no later structures in the area appear to have modified these surfaces. The topographic slopes of 41.6° + 5.5°/−3.5° for the west facing surface (east side) and 14.5° + 21.8°/−11.6° for the east facing surface (west side) are significantly lower than the ~65° dip expected from Anderson's theory of faulting, which treats normal faults as Coulomb fractures. Substantial evidence suggests that unmodified, upper crustal normal faults on the Earth do approximate this orientation [*Suppe*, 1985; *Walsh and Watterson*, 1988]. The slope of the west facing surface is, however, within the 31°–39° range expected for a scree slope of well-drained, unconsolidated materials [*Chandler*, 1973; *Selby*, 1993]. Although the east facing surface has a significantly lower slope, the high measurement uncertainty of the slope indicates that it could also represent a scree slope. If the slope is, in fact, closer to the measured 14.5° topographic slope, then the surface is more likely a fold limb or the result of multiple, closely spaced, small faults.

It seems reasonable that the graben in Figure 10 is bounded by a normal fault on at least one side. The asymmetric topography suggests that the east side is a likely candidate for a fault-related surface. Because the ~42° slope of the east side is substantially lower than the Coulomb-fracture orientation of 65°, we propose that the topographic slope of the face represents a scree slope and that the region around the fault has little cohesive strength. We believe that there are only two reasonable subsurface interpretations for the west side of the trough: (1) the graben is bounded by one, or more, antithetic normal faults with less slip than the eastern fault, and which have also collapsed to a scree slope, or (2) the graben is bounded by an extensional fold limb with perhaps a lower topographic slope. We balance the first interpretation through simple rigid-body translation along fault planes and balance the second by using fault-related folding theory [*Xiao and Suppe*, 1992] (Figure 11). For simplicity, we model the surface prior to deformation and the present shape of the floor of the graben as horizontal in both cases. As mentioned earlier, analysis of the SAR images shows that the graben cuts earlier positive-relief wrinkle ridges, including some within the floor of the graben, and so a horizontal assumption is not completely accurate. However, we calculated a gentle 1.9° + 4.2°/−3.3° slope to the floor of the graben that within the uncertainty of the measurement could be horizontal. Thus we believe that a horizontal floor to the graben is a good first-order approximation of the geometry and simplifies our interpretation below.

The actual positions of the faults are, of course, unknown. Theoretical models of talus slope formation from collapsed rockwalls predict a convex shape to the rock slope mantled by talus, with the original position of the rock wall closer to the crest of the talus slope than the base [*Fisher*, 1866; *Lehmann*, 1933], but little evidence exists to support such models [*Selby*, 1993]. We assume that faults lie in the middle of their corresponding talus slopes. Because there is no erosion, no removal of material from the base can occur. This implies that no void space is created by secondary fracturing, which is, of course, a simplification. Volume increase from solid rock to scree may be >20%, but within the uncertainty in which we know the orientation of the face, we believe that assuming no increase in volume is permissible. Because there is no erosion, the height of a tallus slope is equal to the throw on the underlying fault and thus constrains slip on the faults. On Venus, lava flows could fill in a graben, but we do not see any evidence for postdeformation lava flows in this area, given the prefaulting wrinkle ridges.

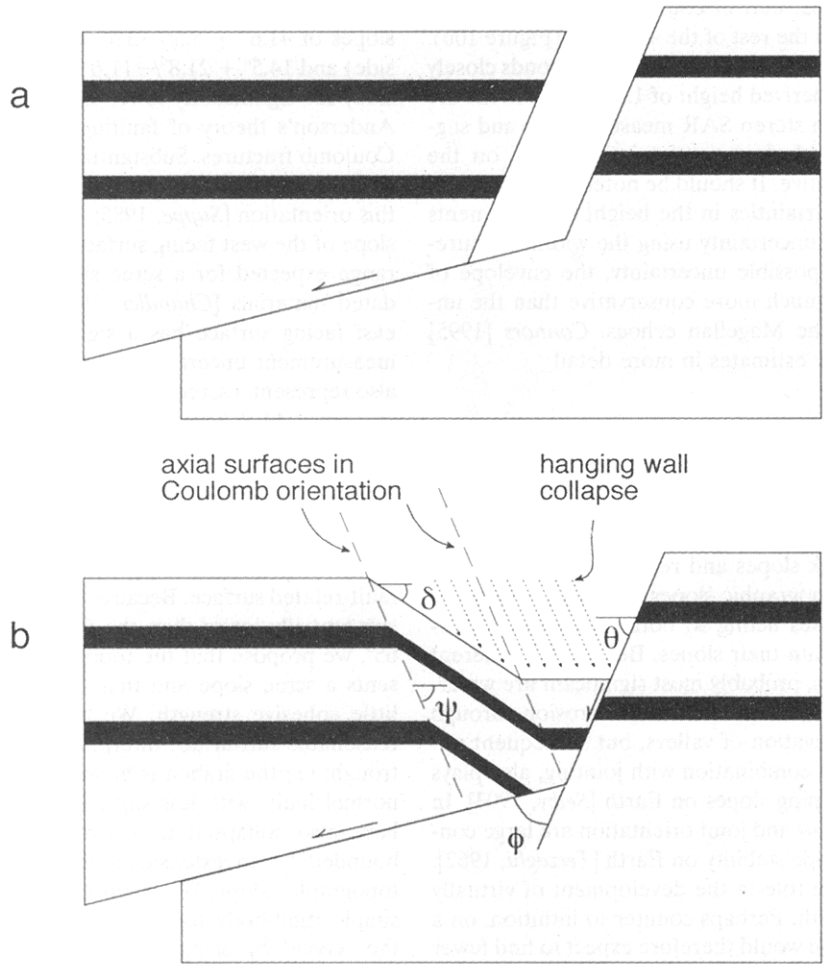

Figure 11. Extensional fault-bend folding [after *Xiao and Suppe*, 1992]. (a) Displacement on shallower dipping fault segment creates unreasonable void near the more steeply dipping segment of the fault. (b) Accommodation of different displacements on different segments of nonplaner fault by collapse of the hanging wall to fill the void. Model is area balanced. That is, no area is lost during faulting and folding. Relationship of fold shape, ψ and δ, to fault shape, θ and ϕ, is given in (5).

If the graben formed from opposing normal faults, then the two faults must displace each other at depth. Of course, the order of faulting is not known. If we assume that the dip of both faults is 65°, and they are located in the middle of their respective scree slopes, we can displace the hanging wall blocks in turn the appropriate amount to accommodate the throw on both faults and develop the balanced model shown in Figure 12a. This prospect does not lend itself to testing since we do not have subsurface data. In addition, the solution requires that the actual slope of the east facing surface is at the upper limit of our measurement uncertainty. However, multiple antithetic faults (below the resolution of the radar) could produce a lower overall slope, depending on their spacing. Invoking multiple faults of proper spacing to exactly fit the observed overall slope is somewhat arbitrary and is not particularly enlightening because there is no additional test of the validity of such a model. However, a fold limb generated in fault-bend folding is essentially one end-member to this multiple fault solution and is a testable solution which we explore below.

Fault-bend folding theory assumes that displacement occurs parallel to fault surfaces, with rigid-body translation occurring in the hanging wall except at fault bends. Displacement is accommodated in the hanging wall by folding as material passes through faults bends (Figure 11). Using the fault-bend folding relations, solutions are area balanced. In extensional fault-bend folding this process can be thought of as collapse of the hanging wall to fill the void created near the more steeply dipping segment of the fault by displacement on a shallower dipping segment [*Xiao and Suppe*, 1992] (Figure 11). Vertical and inclined collapse directions have been used, but most workers now favor an antithetic normal fault orientation [*Groshong*, 1989; *Dula*, 1991; *Xiao and Suppe*, 1992]. Use of a 65°–70° antithetic direction is termed Coulomb collapse by *Xiao and Suppe* [1988] and is particularly appealing because the maximum compressive stress in extensional tectonics is essentially vertical [*Xiao et al.*, 1991]. Thus a Coulomb-shear direction of collapse is analogous to Anderson's predictions of fault orientation based on principal stress orientations. Experimental analog models and seismic reflection data have shown that these fold limbs are, in fact, composed of many small faults [*Cloos*, 1968; *Xiao and Suppe*, 1992; *Withjack et al.*, 1995].

Fault-bend folding relates the fault shape to the fold shape, which in extensional fault-bend folding is given by

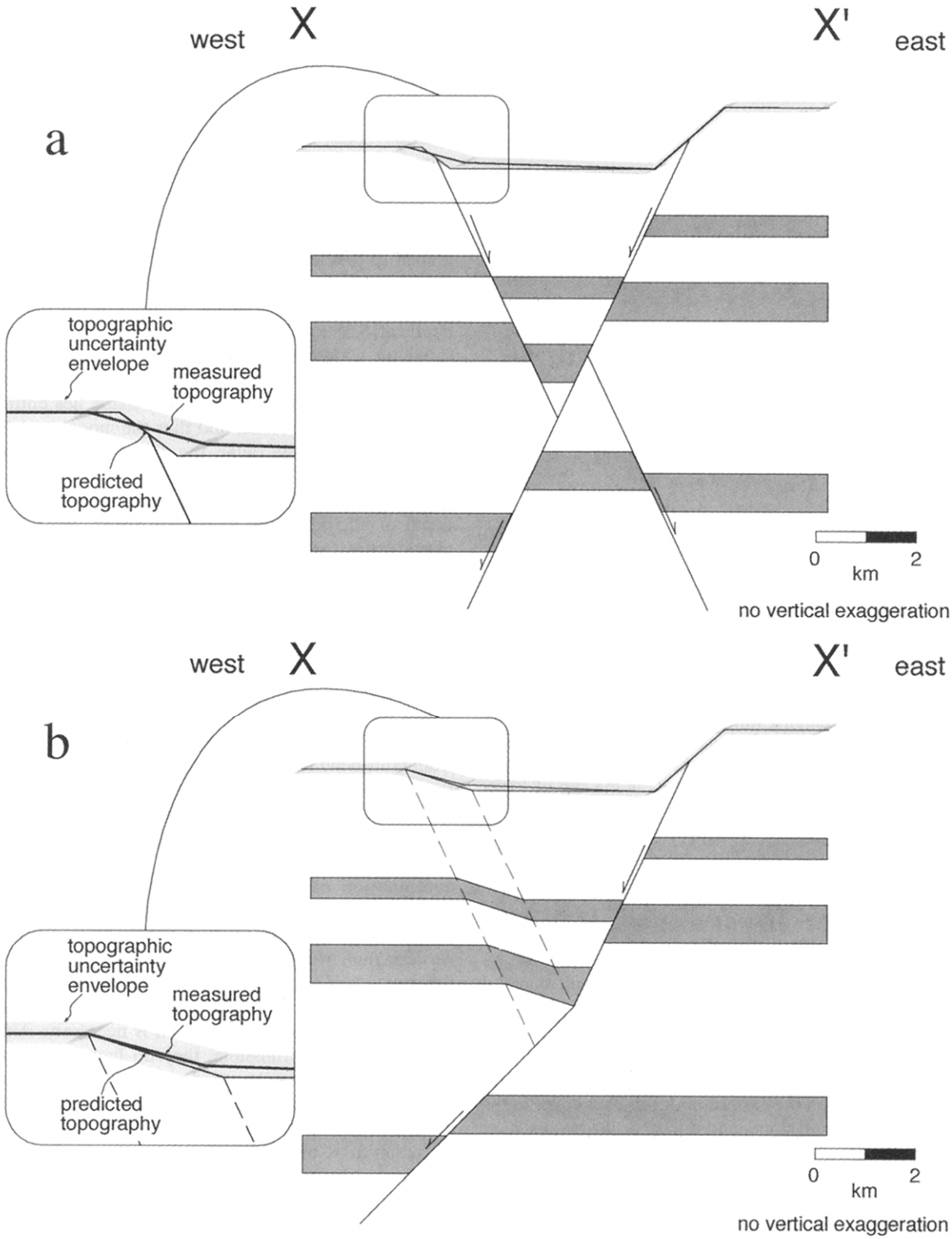

Figure 12. Two alternative balanced cross sections of the graben shown in Figure 10. The topographic slope of the east side suggests a tallus slope, whereas the slope of the west side may represent primary extensional fold limb dip or a tallus slope also. Neither side is interpreted to represent primary fault geometry; see text for discussion. (a) Two-fault solution, where one fault cuts other at depth. (b) Fault-bend fold solution, where a bend in fault at depth is accommodated at the surface through folding. The slip on fault is used to predict fold shape of the west side. Total extension across the graben in either solution is 780 m.

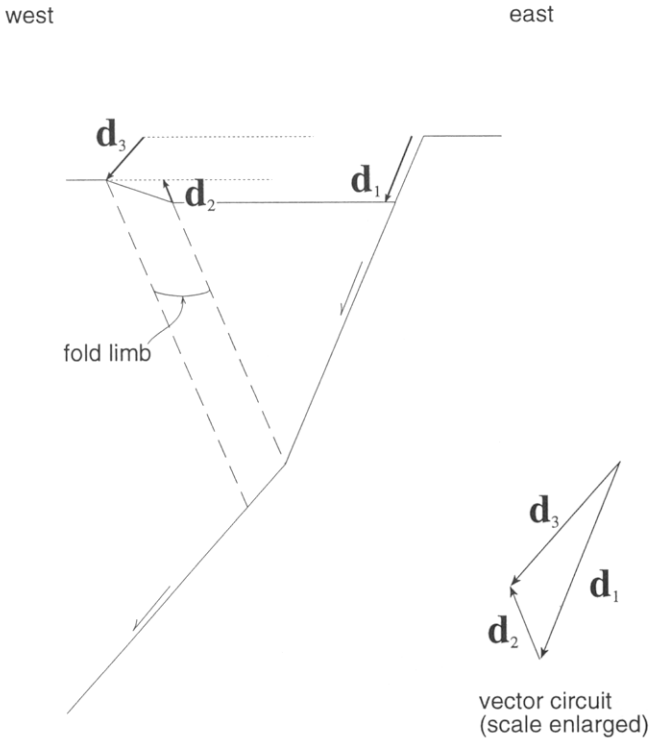

Figure 13. Use of displacement vectors to construct fault-bend folding solution shown in Figure 12b. The slip on the eastern fault is used to predict fold shape of the west side. Assumptions were a Coulomb-collapse angle for folding and Coulomb-shear angle for upper fault orientation. The displacement of the hanging wall west of the fold limb relative to the footwall is the vector sum, $\mathbf{d}_3 = \mathbf{d}_1 + \mathbf{d}_2$, where $\mathbf{d}_1$ is the displacement of the hanging wall east of the fold limb relative to the footwall and $\mathbf{d}_2$ is the displacement of the hanging wall west of the fold limb relative to the hanging wall east of the fold limb. Note that the orientation of $\mathbf{d}_3$ is the dip of lower fault segment.

$$\frac{\sin\psi \sin(\psi - \delta)}{\sin(\theta + \psi - \phi)\sin(\theta + \psi)} = \frac{\sin\delta}{\sin\phi}, \tag{5}$$

where θ is the cutoff angle between the undeformed surface and the upper fault segment, ϕ is the change in fault shape, ψ is the collapse direction, and δ is the dip of fold limb [*Xiao and Suppe*, 1992] (Figure 11). Even with assumptions for θ and ψ, we still have two unknowns, ϕ and δ, and thus cannot directly solve for the shape of the graben in Figure 10 using (5). What we know is the throw on the eastern fault, which is equal to the height of the west facing slope, and the vertical separation, or "throw," the hanging wall block has experienced east of the crest of the east facing surface, which is equal to the height of the east facing slope (Figure 13). With this information we can use the slip on the eastern fault to predict the shape of the western fold limb, δ. If we assume that the dip of the eastern fault $\theta = 65.0°$ and that its location is in the middle of the eastern scree slope, we can displace the hanging wall block parallel to the fault the appropriate amount, $\mathbf{d}_1$, to accommodate the throw on the eastern fault of 1240 m. If we assume an antithetic Coulomb-collapse angle of $\psi = 65.0°$ for the dip of the axial surfaces, we displace the hanging wall block west of the fold limb an appropriate amount, $\mathbf{d}_2$, to accommodate the vertical separation of 432 m relative to the hanging wall block east of the fold limb. The sum of the two displacement vectors, $\mathbf{d}_1 + \mathbf{d}_2$, is the displacement of the hanging wall west of the western fold limb relative to the footwall, $\mathbf{d}_3$, which is parallel to the dip of the lower bend in the fault (Figure 13). Thus the direction of $\mathbf{d}_3$ is the dip of the lower fault segment, $\theta - \phi$, which in this case is 46.0°. Now we can use (5) to directly solve for the predicted dip of the fold limb, δ, on the west side of the graben. Our solution of $\delta = 17.7°$ is close to the measured 14.5° + 21.8°/−11.6° slope of the west side of the graben and lends support to this model. If we assume that the crest of the east facing surface represents the position of the anticlinal axial surface and assume a flat-lying graben floor, we can extend the fold limb from the crest of the face at 17.7° to the floor of the graben to predict the location of the synclinal axial surface of the fold limb. Projection of the synclinal axial surface from the surface to the fault yields the location of the fault bend at a depth of 5.55 km below the top of the footwall. Figure 12a shows the good correspondence between the model prediction of the topography and that of the topography derived from the radar images. Note that the model shape lies entirely within the uncertainty envelope, and thus the model explains, within the resolution of the radar, the measured topography of the graben.

The change in fault dip from the modeled 65° to 46.0° at a depth of 5.55 km is an interesting result. Below the brittle-plastic transition, there is no pressure dependence, and thus in homogeneous media one predicts a fault dip of 45°. These results therefore suggest that the brittle-plastic transition may have been between 5–6 km at this location on Venus when the deformation occurred. Alternatively, the deeper fault shape may be a result of some preexisting weak surface (e.g., an old rotated fault), but a dip of 45° would have to be considered a coincidence.

The predicted dip of the west side of the graben derived from fault-bend folding theory provides internal consistency to the idea that the western face of the graben constitutes an extensional fold limb. A single fault solution is also consistent with the geology of the area because the eastern fault is the outermost fault of a rift system in this area (Figure 4). Thus continuation of this fault to the west seems reasonable, whereas continuation of an east vergent fault presents the problem of where slip goes at depth. Since the throw on a western fault would be 432 m, one could presume that this deformation is accommodated elastically over a much larger region than this graben. However, with the fault-related folding solution, no such presumption is necessary. Although either solution is permissible, they do have different implications, and neither can be ruled out given the present data. We presented alternative solutions to show that it is entirely possible, and in fact probable, that some of the slopes visible in Magellan SAR over areas that appear to be extensional may not be directly related to faults, but rather may be discrete, extensional fold limbs.

Interestingly, if one wishes to know the extension across the graben, it does not matter which solution, fault or fold, is employed because extension is equal in both cases. A consideration of the displacement vectors is once again needed to understand why this is so. For both cases, $\mathbf{d}_1$ is, of course, the same, and thus the extension (the horizontal component of $\mathbf{d}_1$) related to displacement on the eastern fault is the same in either solution (Figure 14). Likewise, because we assumed for the east facing surface of the graben a Coulomb-collapse angle in the fault-bend folding solution and a Coulomb-fracture ori-

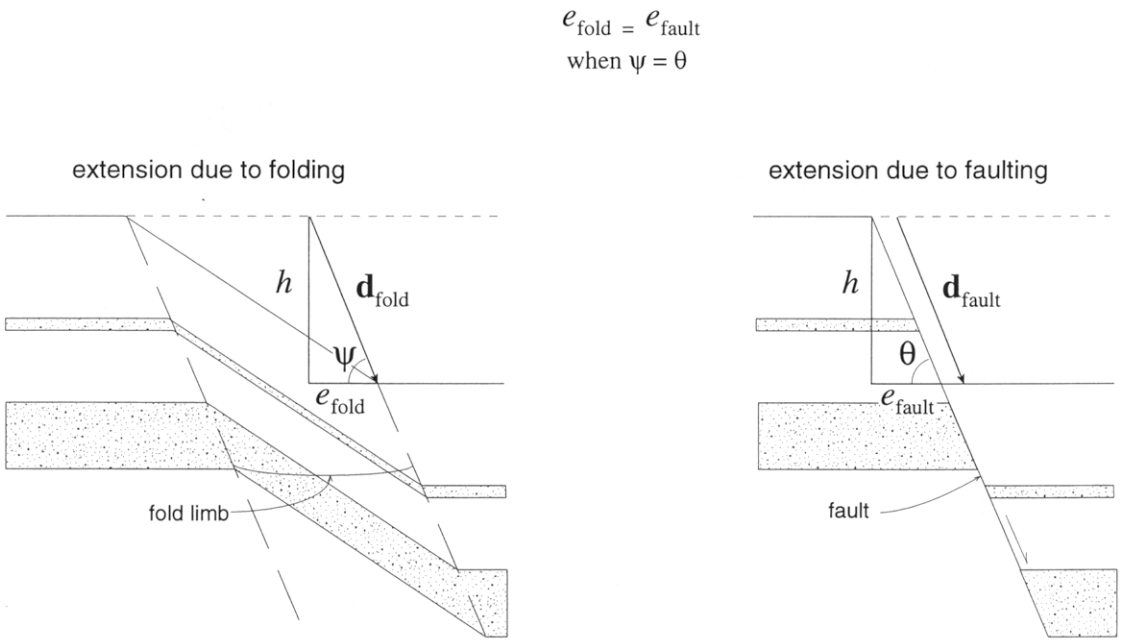

Figure 14. Extension related to faulting, e_{fault}, is the horizontal component of the displacement vector $\mathbf{d}_{fault}$. Likewise, extension related to folding, e_{fold}, is the horizontal component of the displacement vector $\mathbf{d}_{fold}$. Because surface slopes on Venus do not generally reflect primary fault orientation, the most important constraints on subsurface structural geometries are heights of surfaces. Because we assume a Coulomb-shear angle for fault orientation, θ, and a Coulomb-collapse angle for folding, ψ, that is, $\psi = \theta$, extension will be the same, $e_{fold} = e_{fault}$, in either the folding or faulting solution for a given surface height. The width of the deformation zone does not affect extension across the surface.

entation in the two-fault solution, $\mathbf{d}_2$ will be the same for both cases because $\psi = \theta = 65°$ (Figure 14). Thus the displacement of the hanging wall rocks west of the western fold limb relative to the footwall is the same in either solution, $\mathbf{d}_3 = \mathbf{d}_1 + \mathbf{d}_2$, and thus the horizontal component of this will be the same in either solution, $e = 780$ m. One way to consider the fold limb is as multiple, closely spaced faults which terminate at the fault bend and over which deformation is distributed, as opposed to discrete displacement on one fault. The width over which deformation occurs does not affect the amount of extension, only the throw and fault or axial surface orientation.

We presented the detailed treatment of this particular graben to show that because of the lack of erosion on Venus, it is possible without stratigraphic or subsurface information to constrain subsurface structural geometries, if surface topography is known in enough detail. Unfortunately, most structures are not imaged nearly as well in Magellan SAR as the graben in Figure 10. In the 20% of the planet covered with stereo SAR, none of the major extensional zones were adequately imaged in stereo, much less in all three cycles. Nonetheless, many individual surfaces related to normal faulting were imaged with stereo SAR, and with these images we can determine how representative the graben in Figure 10 is of surfaces related to normal faulting on Venus.

4. Mean Slope Related to Normal Faulting

4.1. Method

Have most normal faults on Venus collapsed to tallus slopes? In an effort to answer this question, we calculated the topographic slope and height of 170 discretely dipping surfaces within plains terrains of Venus that we interpreted as being related to normal faults on the basis of the geologic criteria discussed above. We measured the widths of the surfaces imaged in Magellan stereo SAR and used (2) and (3) to determine the slope and (4) to determine the height of the surfaces as described above and by *Connors* [1995]. We incorporated additional information, such as cycle 2 images, Magellan altimetric echos, or stereoscopic impression, to uniquely determine the imaging of a surface. In this analysis, if the imaging domain of a west facing surface could not be uniquely determined because of a lack of additional information, then we excluded that surface from the sample.

Surfaces were measured that faced both west and east, that had a variety of strikes, and that spanned most of the latitude range of the stereo SAR data set (Figures 15 and 16). Criteria for the measurements were that the surface be well imaged in both cycle 1 and 3 SAR, be separated by >3.5 km from an adjacent measured surface, and be >350 m (approximately twice the average range resolution of the SAR) in width in both images. This last criterion was to limit any possible bias associated with the spatial resolution of the radar. In addition, we were interested in the slope of isolated surfaces and thus excluded slopes that appeared to be part of a multiple fault system or polydeformed. An example of polydeformed faults, in this case from a rotated fault-block system, that were excluded from the sample are those shown in Figure 10 of *Connors* [1995]. Other examples that would not qualify are most of the intensely deformed terrain of Figure 6 and all of the tessera terrain.

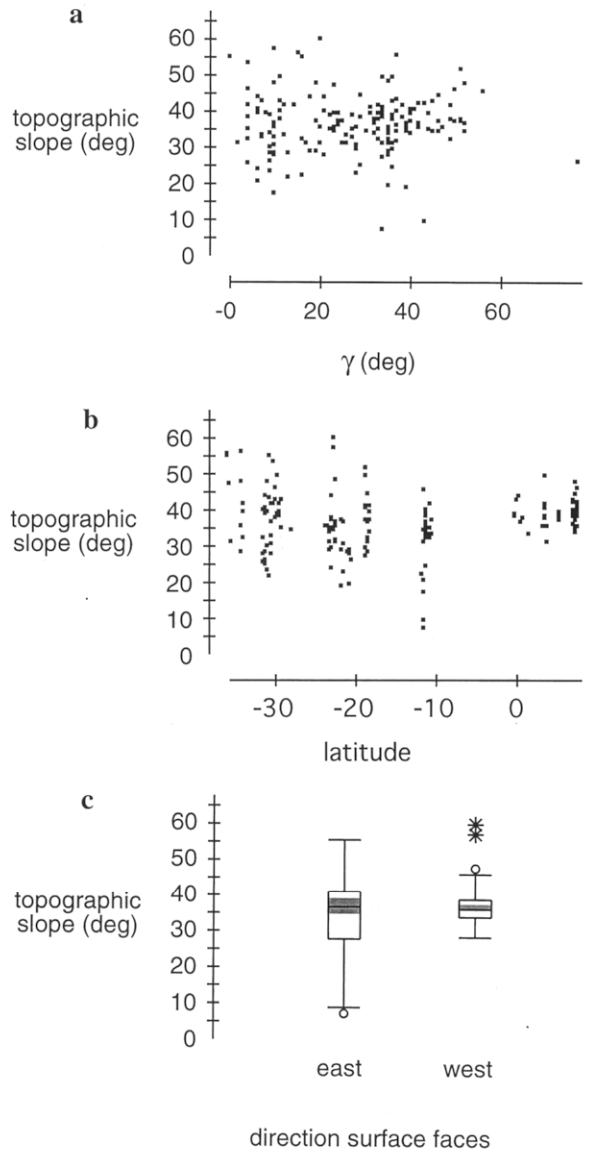

Figure 15. (a) Plot of topographic slope for nonimbricated surfaces related to normal faults on Venus relative to the small angle between the strike of the face and the radar azimuth direction, γ. The scatterplot shows that there is no trend between γ and the topographic slope, indicating that no bias is being introduced by the strike of a surface. (b) Plot of topographic slope for nonimbricated surfaces related to normal faults on Venus relative to latitude. The scatterplot shows that there is no trend between the topographic slope and the latitude of the surface, indicating that no bias is being introduced by the latitude of a surface. (c) Box-and-whisker plot of topographic slope for nonimbricated surfaces related to normal faults on Venus relative to the orientation the surface faces. The box-and-whisker plot shows that the means of the two face orientations are indistinguishable, indicating that no bias is being introduced by surface orientation. The shaded box is the 95% confidence interval based on t distribution. The horizontal bar is the median, the box hinges are at roughly 25 and 75 percentiles, the whiskers are a representation of the normal range of the data, and the circles and stars represent extreme values relative to distribution.

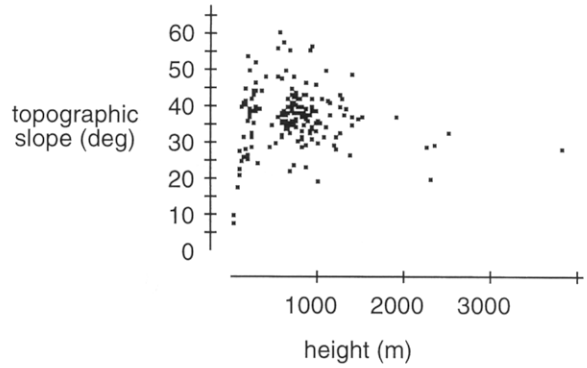

Figure 16. Plot of topographic slope for nonimbricated surfaces related to normal faults on Venus relative to the height of the surface. The scatterplot shows that the topographic slope is independent of the height of the surface.

4.2 Results

Table 1 summarizes the sample data for the topographic slopes. The sample has a mean topographic slope of 36.4° ± 1.2°, where the limits represent the 95% confidence interval based on the t distribution. The approximately linear normal probability plot and characteristic bell-shaped histogram indicate that the sample approximates a normal distribution (see Figure 17) with closely coincident median and mean, but there is a slight negative skewness and positive kurtosis to the distribution. Nonetheless, we believe that the data are close enough to normally distributed that using parametric statistics is permissible.

We were interested in whether there was bias in the sample due to strike of the face relative to the radar azimuth direction (γ in Figure 9) or incidence angle of either the cycle 1 or cycle 3 images (a function of latitude in Magellan SAR). Regression of topographic slope on gamma and latitude give low t ratios (Table 2), indicating at the 95% confidence level that the null hypothesis $\beta = 0$ is accepted, where β is the slope of the regression line. Thus we conclude that there is not a bias in the sample mean being introduced by the continuous variables. Inspection of the scatterplots in Figures 15a and 15b qualitatively confirms this conclusion.

We also explored the possibility of a bias due to face orientation (Figure 15c). These box-and-whisker plots [*Tukey*, 1976] graphically summarize information about the distribution of the sample with respect to the discreet variable face orientation. The shaded box is the 95% confidence interval based on the t distribution. The horizontal bar is the median of the sample, whereas the box hinges are at roughly 25 and 75 percentiles. The whiskers are a representation of the normal range of the data, and the circles and stars represent extreme values relative to the distribution. Using a pooled t test to look

Table 1. Summary Statistics for Sample Topographic Slopes Related to Normal Faulting on Venus

Item	Value
Mean	36.4° ± 1.2°[a]
Median	36.8°
Standard deviation	8.2°
Numeric	170

[a]The 95% confidence interval based on t distribution.

for significant differences in the sample due to face orientation, we find that at the 95% confidence level the null hypothesis $\mu_{west} - \mu_{east} = 0$ is accepted (Table 3), where μ signifies the mean. This can also be seen graphically in Figure 15c because the shaded regions of the box-and-whisker plots between the west and east faces overlap. With no significant difference between the means of the face orientation, we conclude that there is not a bias in the sample mean being introduced by the orientation of the face. Interestingly, however, there is more dispersion, or a larger standard deviation, in the east facing surfaces, that is, $\sigma_{west} > \sigma_{east}$. This greater variation in the slopes of east facing surfaces can be seen graphically as larger whiskers and boxes than for west facing surfaces in the box-and-whisker plots of Figure 15c. We believe that this represents the larger measurement uncertainty associated with calculating east versus west facing surfaces when using this measurement technique, as described above (Figure 8) and by *Connors* [1995].

Because the technique used to calculate topographic slope also calculates the height of the surface, we were able to test whether there was any linear relationship between the topographic slope and height of the surfaces. Unlike with gamma and latitude above, this was motivated from a geologic perspective to see if the height of a surface was an adequate predictor of the slope of the surface. Regression of topographic slope on the calculated height gives a low t ratio (Table 2), indicating that at the 95% confidence level the null hypothesis $\beta = 0$ is accepted. Thus we conclude that there is no significant linear relationship between height and topographic slope in the sample. Inspection of the scatterplot in Figure 16 qualitatively confirms this conclusion.

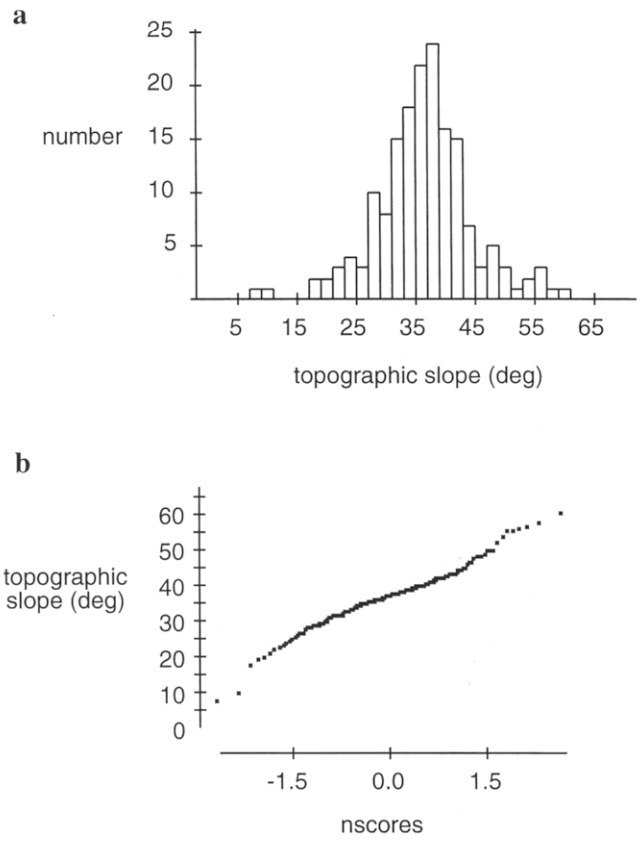

Figure 17. (a) Histogram and (b) normal probability plots of topographic slopes for nonimbricated surfaces related to normal faults on Venus. Nscores equal standard deviation.

Table 2. Regression Analysis for Sample Topographic Slopes Related to Normal Faulting on Venus[a]

Variable	Degrees of Freedom	t Ratio	Probability
Gamma	168	0.24	0.81
Latitude	168	0.52	0.60
Height	168	−0.55	0.58

[a]Significance level for the probability was 0.05.

4.3. Interpretation

We believe that the mean slope of the sample, 36.4° ± 1.2°, is a good description of the mean slope of nonimbricated, nonpolydeformed surfaces related to normal faulting on the surface of Venus. The mean slope is within the range expected for noncohesive or scree hard rock slopes on Earth [*Selby*, 1993]. Because there is little to no erosion on Venus, we interpret this mean slope to represent primarily talus slopes from collapsed fault scarps, approximately at an angle of repose, and not an indication of primary normal fault geometry. Although the undeformed upper crust of Venus probably has high inherent cohesive strength, these data suggest that in general the crust immediately adjacent to normal faults on Venus has little, if any, cohesive strength, probably because of secondary faulting and jointing. The lack of a significant linear relationship between the height and topographic slope in the sample supports this conclusion. One would expect a decrease in slope with increasing height if there were some residual cohesive strength to the faulted surfaces.

The distribution in the population of surfaces on Venus related to normal faulting is certainly more complicated than the sample population. Although we limited our sample to those we interpreted as normal fault-related, it is possible that some of the lower topographic slopes may reflect dips of extensional fold limbs. We did not attempt to separate fold limbs from collapsed fault scarps. As with the example in Figure 11, it is probably not possible to do so in most cases. Likewise surfaces that maintain some cohesive strength should have topographic slopes that are higher than the angle of repose, and thus some of the steeper topographic slopes in the sample may reflect maintenance of significant cohesive strength around some faults. In addition, we tried to pick unambiguous, apparently nonimbricated slopes, but later folding or faulting not visible in the images may contribute to variability in the sample. With regard to face orientation, variance in the sample may be partially due to measurement uncertainty. Nonetheless, we believe that this mean slope can provide a useful first-order

Table 3. Pooled t Test for Sample Topographic Slopes Related to Normal Faulting on Venus[a]

Item	Value
Test	$\mu_{west} - \mu_{east} = 0$
Difference between means	−1.5
t statistic	−1.2
Degrees of freedom	168
Probability	0.24

[a]Significance level for the probability was 0.05.

bound on estimates of extension across rift zones, as discussed below.

5. Estimates of Extension Across Rift Zones

5.1. Method

The spectacular rift zones of Venus are interesting to investigators because they are apparently the largest extensional regions on Venus. Thus estimates of extensional strain accommodated by structures apparent in these zones should provide first-order constraints on global tectonic models of Venus. The most satisfying estimates of extension across these zones would probably be based on balanced cross sections, using methods such as those used for the individual graben in Figure 10. Unfortunately, the rift zones were imaged only in cycle 1 SAR; thus we cannot use these techniques to rigorously determine extension. We can, however, use the mean slope for surfaces related to normal faulting that we determined for areas of the planet imaged in multicycle Magellan SAR, along with the widths of the faces in cycle 1 images, to estimate extension across a particular rift zone at a particular transect as follows. Rearranging (1) for the height of a surface, we get

$$h = \frac{w \tan \Omega \tan \alpha}{(\tan \Omega \pm \tan \alpha)}. \tag{6}$$

We can solve the height relative to the true topographic slope α_{true} by substituting (3) into (6) to get

$$h = \frac{w \tan \Omega \tan \alpha_{true} \cos \gamma}{(\tan \Omega \pm \tan \alpha_{\text{true}} \cos \gamma)}. \tag{7}$$

From Figure 14 we see that the extension e is related to this same height, or throw, and fault orientation θ by

$$e = \frac{h}{\tan \theta}. \tag{8}$$

Note that if extension is accommodated over a fold limb rather than a fault, then the collapse direction ψ can be substituted for θ (see Figure 14). Since we want the extension in the dip direction across one imaged fault, we can substitute (7) into (8) to get

$$e = \frac{w \tan \Omega \tan \alpha_{true} \cos \gamma}{\tan \theta (\tan \Omega \pm \tan \alpha_{\text{true}} \cos \gamma)}. \tag{9}$$

Summing the extension on all imaged faults, or fold limbs, gives the total extension across a rift zone, e_{rift}, at one transect normal to the general trend of the rift through the relation

$$e_{\text{rift}} = \sum_{n=1}^{n} \frac{w_n \cos\gamma_n^* \tan \Omega \tan \alpha_{\text{true}} \cos \gamma}{\tan \theta (\tan \Omega \pm \tan \alpha_{\text{true}} \cos \gamma)}, \tag{10}$$

where γ^* is the acute angle between the general trend of the rift zone and the strike of each surface. The use of γ^* gives us the slip component perpendicular to the general trend of the rift zone along each fault; we assume only dip-slip motion on the faults. The sign in (10) is positive for east facing surfaces and negative for west facing surfaces. Depending on latitude and strike, the imaged surface may be laid over or foreshortened; thus consideration of the strike of the face must be made to determine the imaging of a surface and thus the sign of w (Figure 9). With (10) we can make first-order estimates of extension across a rift zone in terms of parameters on which we can place reasonable bounds, θ and α_{true}, or that we can measure, w, γ^*, γ, and Ω.

5.2. Example

The spectacular deformation belt in the Beta Regio region of Venus known as Devana Chasma was interpreted as extensional in origin on the basis of analysis of Pioneer Venus SAR and altimetry [*McGill et al.*, 1981], along with more recent analysis of Magellan SAR and altimetry [*Solomon et al.*, 1992; *Senske et al.*, 1992]. Using the criteria discussed in the section on structural interpretations of SAR (section 2.1), such as the observation that the negative-relief features are through-going, we concur that the zone is extensional in origin. The rift zone cuts two regional highs, Rhea and Theia Mons, as well as volcanic plains in between these mountains. Using (10), we estimated the extension across the north-south trending rift zone at three transects at latitudes 15.0° N, 18.6°N, and 28.6°N (Figures 18 and 19). We assumed a Coulomb-fracture orientation for the fault dip or fold limbs, $\theta = \psi = 65°$, and used the mean topographic slope for surfaces related to normal faulting estimated above, $\alpha_{\text{true}} = 36.4°$. Inspection of Figure 9 shows that for cycle 1 images between 40°N and 20°S latitude, slopes of 36.4° were foreshortened for all strikes. The three transects all lie within this latitude range, and thus w was positive in (10). We chose transects across the rift zone in the volcanic plains, where discretely dipping surfaces were most clearly imaged and where the assumption of a mean slope of 36.4° was most appropriate, that is, where there are little apparent polydeformed slopes. We chose areas where the graben appeared to cut all previous geologic features such as volcanic flows in order to minimize error associated with flooding of graben. As with our determination of the mean slope above, we chose to exclude measured surface widths <350 m to minimize resolution-related artifacts.

5.3. Results and Uncertainty Estimates

Uncertainties in extension estimates derived from (10) are a function of measurement uncertainties in w, γ^*, γ, and Ω. Because we can measure the strike of a surface accurately, the errors in these measurements are generally second-order. Thus we assume measurement uncertainties of the strike of a face $d\gamma^* = d\gamma = 0$. Likewise, the uncertainty in the nominal incidence angle is negligible, so we assume $d\Omega = 0$. The uncertainty in the width measurement, dw, is equal to the range uncertainty of Magellan radar [*Connors*, 1995]. The range uncertainty varies with latitude, and for the three transects of interest here, $dw = \pm 101$–$107\ m$ [*Sanders et al.*, 1992].

Implicit in our derivation of (10) is the assumption that any deviation for an individual surface from a chosen θ or α_{true} will be averaged out by deviations from other surfaces within the transect. In other words, our choices of θ and α_{true} are really average values since we cannot directly determine these for an individual surface. Thus the uncertainty in the total extension in (10) is related to the uncertainty in the average θ or α_{true} we assume. We believe that a sensible uncertainty in α_{true} is the 95% confidence interval derived for topographic slope from stereo measurements of surfaces related to normal faulting (Table 1), or $d\alpha_{\text{true}} = \pm 1.2°$. Uncertainty in θ is more difficult to quantify. One truly end-member minimum solution is that $\theta \geq 45°$ in order to maintain the assumption of the fault plane being a Coulomb-fracture orientation with a normal sense of displacement; however, this implies that the coefficient of in-

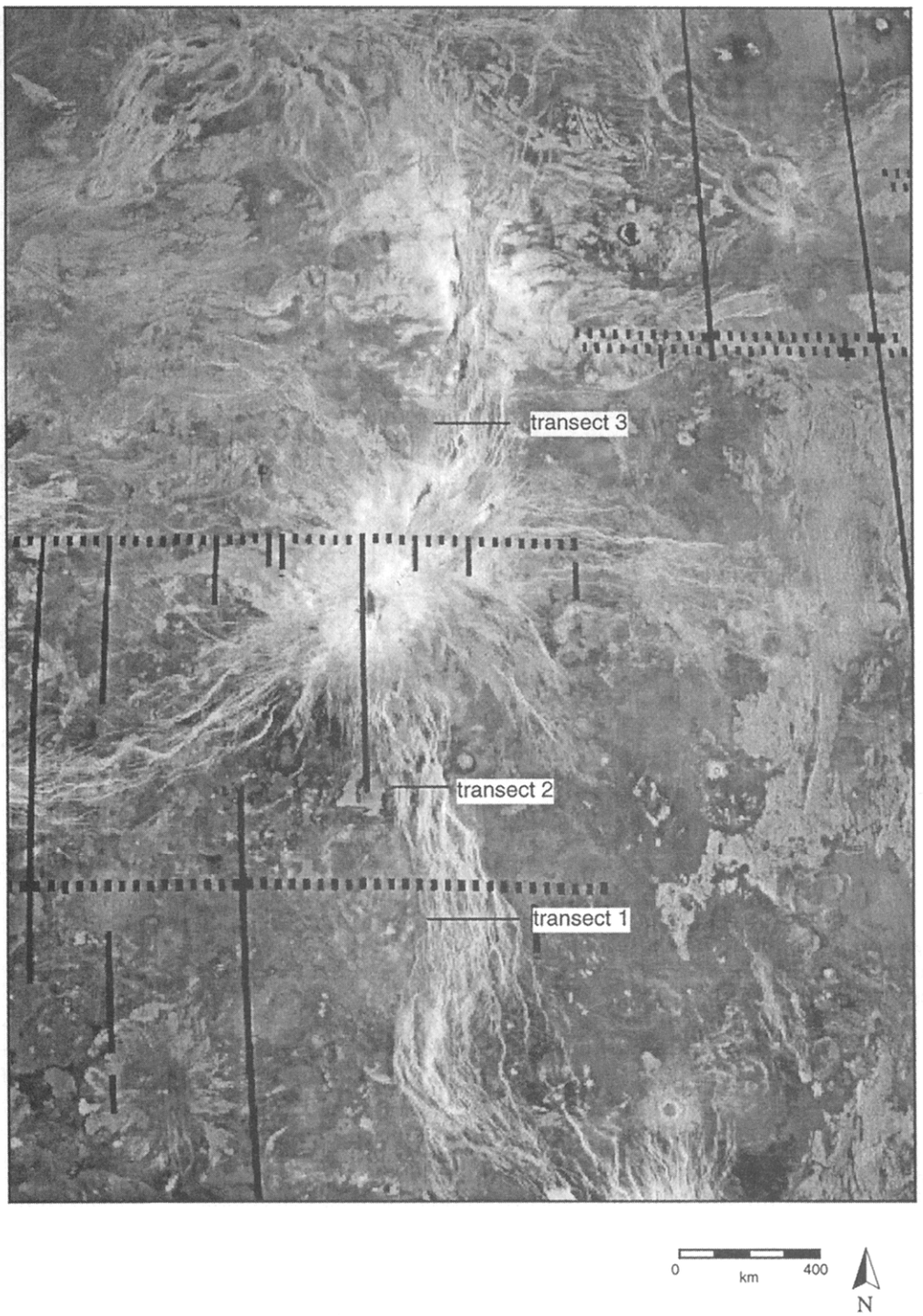

Figure 18. Rift zone across Beta Regio in Magellan cycle 1 SAR image centered at about 20°N, 280° ($\Omega' \approx$ 37°–45°) showing location of three transects where extension was estimated using (10). See Figure 19 for enlargement of transect 1. Interestingly, the spectacular extensional deformation evident in the rift zone is quite modest, from about 8 to 16 km.

ternal friction is negligible, which is unreasonable for any rock type. Perhaps realistic limits to variation in primary normal fault dips on Venus are $\theta = 60°$–$70°$. This range would be consistent with coefficients of internal friction for many rock types on Earth [*Suppe*, 1985] and would encompass most measured dips on normal faults [*Walsh and Watterson*, 1988].

In Table 4 we present extension magnitudes along with uncertainties based on $dw = \pm 101$–107 m and $d\alpha_{\text{true}} = \pm 1.2°$ for a range of fault orientations from $\theta = 60°$, 65°, and 70°. Determining absolute uncertainties in θ is probably not possible at the present time; however, there is utility in presenting extension magnitudes for a range of θ in order to conduct relative comparisons of extension along a rift zone or between rift zones on Venus. For example, for $\theta = \psi = 65°$ the maxi-

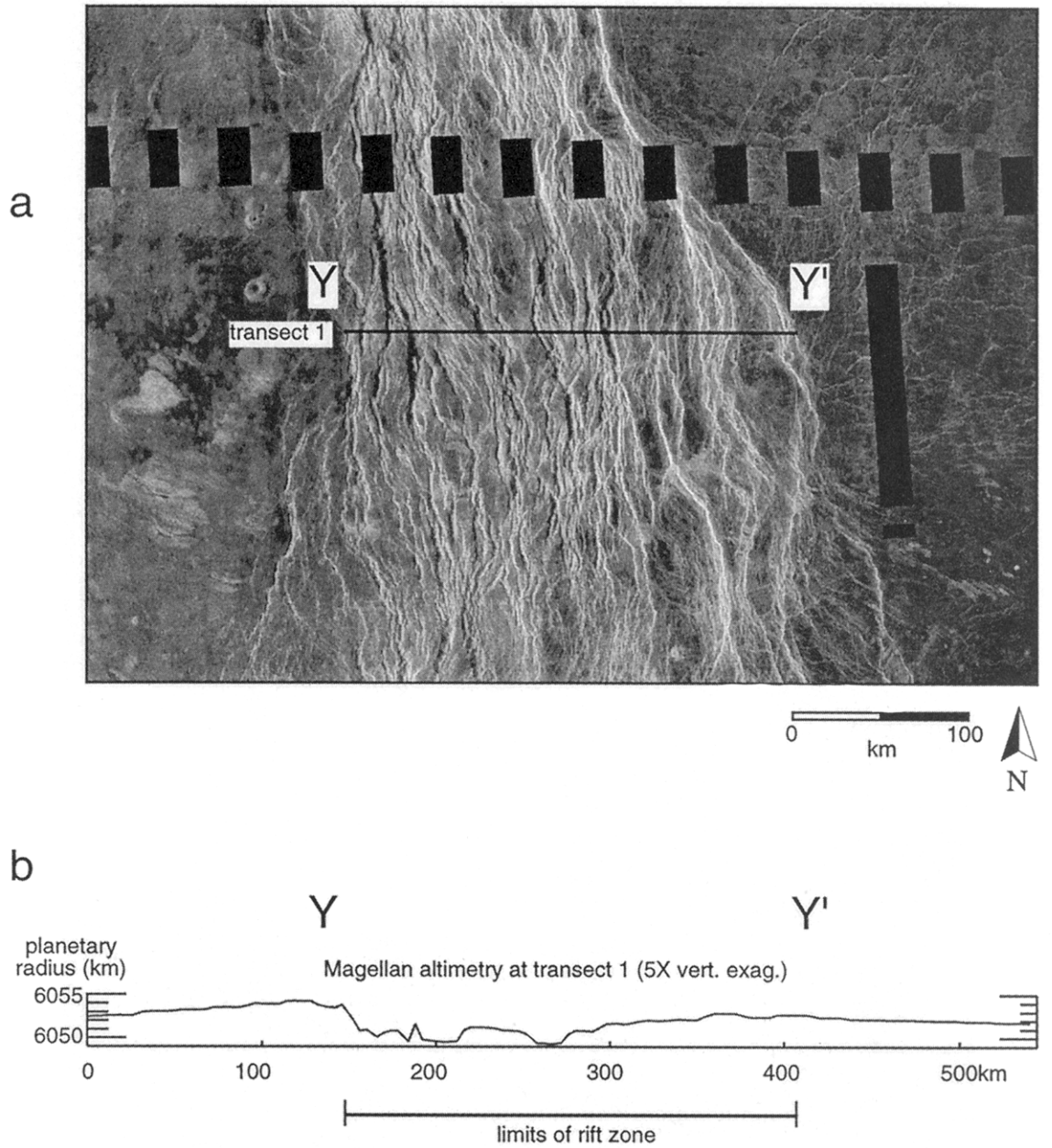

Figure 19. (a) Magellan cycle 1 SAR image at transect 1 across rift zone in Beta Regio (see Figure 18 for location; $\Omega' \approx 45°$). (b) Magellan altimetry across transect 1 showing that deformation is highly correlated to the large-scale topographic depression.

mum estimated extension is 17.6 km +5.6/−4.4 km at transect 1, whereas extension is 9.0 km +2.1/−1.8 km at transect 2 and 16.3 km +6.6/−4.8 km at transect 3 (Table 4). Likewise, a choice of $\theta = \psi = 60°$ yields similar relative extensions between transects although the absolute amounts vary. One additional point should be made with respect to extension uncertainties. These extension estimates may underestimate the greatest extensional strain accommodated across the Beta rift zone because we excluded very small width measurements and because we chose transects that showed little apparent polydeformed slopes. Nonetheless, these first-order strain estimates suggest that extension seems to be relatively small within the Beta rift, consistent with estimates by *Stofan et al.* [1989] and *Senske et al.* [1992].

5.4. Interpretation

Another way to express the strain in these rifts zones is by calculating the stretch S across a transect which is defined as

$$S = L_f/(L_f - e), \tag{11}$$

where L_f is the present length of a transect. For uncertainties in stretch we propagate the extension uncertainty. For $\theta = \psi = 65°$ we get $S = 1.069 + 0.024/-0.018$ for transect 1; $1.063 + 0.016/-0.013$ for transect 2; and $1.081 + 0.036/-0.025$ for transect 3 (Table 4). Within the uncertainties of the method, both stretch and extension are relatively consistent along trend. Consistent stretch with variable extension along trend is more expected if deformation sweeps through the lithosphere such as in kink-band migration of fault-related

Table 4. Estimates of Extension e and Stretch S Across Transects With Length L_f in the Rift Zone in Beta Regio

Transect	L_f, km	e, km	S
		Fault Orientations, θ = 60	
1	270.6	21.8 + 6.9/−5.4[a]	1.087 + 0.031/−0.023[a]
2	155.4	11.4 + 2.7/−2.4	1.079 + 0.020/−0.018
3	218.4	20.2 + 8.2/−5.9	1.102 + 0.047/−0.032
		Fault Orientations, θ = 65	
1	270.6	17.6 + 5.6/−4.4	1.069 + 0.024/−0.018
2	155.4	9.0 + 2.1/−1.8	1.063 + 0.016/−0.013
3	218.4	16.3 + 6.6/−4.8	1.081 + 0.036/−0.025
		Fault Orientations, θ = 70	
1	270.6	13.7 + 4.4/−3.4	1.053 + 0.018/−0.014
2	155.4	7.2 + 1.7/−0.8	1.048 + 0.012/−0.006
3	218.4	12.7 + 5.1/−3.0	1.062 + 0.027/−0.015

[a]Uncertainty based on $dw = \pm 101$ m for transect 1, 102 m for transect 2, and 107 m for transect 3; $d\alpha_{true} = \pm 1.24°$ for all transects.

folds [*Suppe*, 1983]. It is interesting not only that there is a topographic low correlated with the limits of apparent rifting over transect 1 but that this topography is highly asymmetric (Figure 19). As with the topographic trough in Figure 10, we infer from this asymmetry where the major faulting is occurring. In this case, the major faulting appears to lie on the western side of the Beta rift at the latitude of transect 1, and we infer that many of the surfaces on the eastern side of the rift may represent extensional fold limbs. Increased stretch in narrow regions of the rift zone, with consistent extension along trend, is more expected if deformation is localized, with extension over time producing necking of the lithosphere. Thus in order for narrower parts of the rift zone to accommodate the same extension as wider parts, normal faults must be more closely spaced or superposed on earlier faults. A key assumption of the technique, however, is that we are measuring surfaces related to individual normal faults. Thus we preferentially sampled transects where there were little apparent polydeformed slopes, and therefore we are probably not measuring the true extent of necking. With just three measured transects it is not clear which scenario is more probable for the Beta rift zone. More exhaustive measurements along the rift zone are needed to determine the lateral distribution of extension and to refine strain estimates.

These modest strains across one of the best-developed rift zones on Venus put severe limits on tectonic models of Venus, particularly those that invoke significant lateral displacements of the Venusian crust. For example, any type of terrestrial-style seafloor spreading seems precluded. It might be argued that this extension is recording only very recent deformation and that prior to this deformation, the crust was resurfaced in some way, such as flooding by lava, but *Price and Suppe* [1994] calculated the mean age of rifting at about 80 Ma compared to a global mean age of the Venusian crust of about 290 Ma, based on crater densities. Any younger age than this for the rifts, based on the amount of extension measured in this report, is precluded because Price and Suppe used stretch estimates similar to those calculated here, 1.2 ± 0.1 (based on crater ellipticity). That is, if this were just the last of many recent lava flooding/extension sequences, then this would show up as lower crater densities than those observed.

6. Conclusions

Using the stereo SAR data we showed that the mean topographic slope of nonimbricated, nonpolydeformed surfaces related to normal faulting on Venus is 36.4°. We interpreted this mean slope to represent primarily talus slopes from collapsed fault scarps, approximately at an angle of repose, and not an indication of primary normal fault geometry. Although the undeformed upper crust of Venus might have a high bulk cohesive strength, these data suggest that in general the crust immediately adjacent to normal faults on Venus has little, if any, cohesive strength, probably because of secondary faulting and jointing. There were, however, individual surfaces with significantly higher slopes, suggesting that the rocks around some faults may maintain significant cohesive strength. Because most surfaces related to normal faults have collapsed to talus slopes, fault orientation cannot be directly measured. We showed that for grabens well imaged by Magellan stereo SAR, assumption of a Coulomb-fracture orientation for fault dip allows balanced models to be constructed which agree with measured topography across grabens. We made first-order estimates of the strain across the Beta rift zone showing that extension is <20 km, which indicates that at least the most recent extensional deformation accommodated across this rift has been quite modest, with a stretch of 1.06–1.08.

Acknowledgments. This work is supported in part by the Guest Investigator Program of the Magellan Project, NASA-JPL contract 958940, and the Venus Data Analysis Program, NASA-LPI contract NAGW-3706. Allan Rubin read an earlier version of the manuscript. The comments of John Shaw, Jason Morgan, Martha Gilmore, and an anonymous reviewer greatly improved the manuscript. This work benefited from insightful discussions with Frank Bilotti and Jay Lieske. Peter Ford's and Fang Liu's excellent Magellan-related software made extraction and processing of Magellan data much easier.

References

Arvidson, R. E., R. Greeley, M. C. Malin, R. S. Sanders, N. Izenberg, J. J. Plaut, E. R. Stofan, and M. K. Shepard, Surface modification of Venus as inferred from Magellan observations of plains, *J. Geophys. Res.*, *97*, 13,303–13,318, 1992.

Baker, V. R., G. Komatsu, T. J. Parker, V. C. Gulick, J. S. Kargel, and

J. S. Lewis, Channels and valleys on Venus: Preliminary analysis of Magellan data, *J. Geophys. Res.*, *97*, 13,421–13,444, 1992.

Barsukov, V. L., et al., The geology and geomphormology of the Venus surface as revealed by the radar images obtained by Veneras 15 and 16, *Proc. Lunar Planet. Sci. Conf. 16th*, Part 2, *J. Geophys. Res.*, *91*, suppl., D378–D398, 1986.

Basilevsky, A. T., A. A. Pronin, L. B. Ronca, V. P. Kryuchkov, A. L. Sukhanov, and M. S. Markov, Styles of tectonic deformation on Venus: Analysis of Venera 15 and Venera 16 data, *Proc. Lunar Planet. Sci. Conf. 16th*, Part 2, *J. Geophys. Res.*, *91*, suppl., D399–D411, 1986.

Bilotti, F., *Venus Wrinkle Ridges: Structure, Distribution, and Implications for Global Tectonic Evolution*, 191 pp., Ph.D. thesis, Princeton Univ., Princeton, N. J., 1997.

Bilotti, F., and J. Suppe, Planetary distribution and nature of compressional deformation around Artemis Corona, Venus (abstract), *Lunar Planet. Sci., XXIII*, 101–102, 1992.

Campbell, D. B., J. W. Head, J. K. Harmon, and A. A. Hine, Venus: Identification of banded terrain in the mountains of Ishtar Terra, *Science*, *221*, 644–647, 1983.

Chandler, R. J., The inclination of talus, artic talus terraces, and other slopes composed of granular materials, *J. Geol.*, *81*, 1–14, 1973.

Cloos, E., Experimental analysis of Gulf Coast fracture patterns, *Am. Assoc. Pet. Geol. Bull.*, *52*, 420–444, 1968.

Connors, C., Determining heights and slopes of fault scarps and other surfaces on Venus using Magellan stereo radar, *J. Geophys. Res.*, *100*, 14,361–14,381, 1995.

Crumpler, L. S., J. W. Head, and D. B. Campbell, Orogenic belts on Venus, *Geology*, *14*, 1031–1034, 1986.

Drury, S. A., *Image Interpretation in Geology*, 243 pp., Allen and Unwin, Winchester, Mass., 1987.

Dula, W. F., Geometric models of listric normal faults and rollover folds, *Am. Assoc. Pet. Geol. Bull.*, *75*, 1609–1625, 1991.

Fisher, O., On the disintegration of a chalk cliff, *Geol. Mag.*, *3*, 354–356, 1866.

Ford, P. G., and G. H. Pettengill, Venus topography and kilometer-scale slopes, *J. Geophys. Res.*, *97*, 13,103–13,114, 1992.

Frank, S. H., and J. W. Head, Ridge belts on Venus: Morphology and origin, *Earth Moon Planets*, *50/51*, 421–470, 1990.

Ghent, R., and V. Hansen, Structural and kinematic analysis of eastern Ovda Regio, Venus: Implications for crustal plateau formation, *Icarus*, *139*, 116–136, 1999.

Golombek, M. P., J. B. Plescia, and B. J. Franklin, Faulting and folding in the formation of planetary wrinkle ridges, *Lunar Planet. Sci., XXI*, 679–693, 1991.

Grant-Taylor, T. L., Stable angles in Wellington greywacke, *N. Z. Eng.*, 129–130, 1964.

Groshong, R. H., Half-graben structures: Balanced models of extensional fault-bend folds, *Geol. Soc. Am. Bull.*, *101*, 96–105, 1989.

Head, J. W., L. Crumpler, J. Aubele, J. Guest, and R. S. Sanders, Venus volcanism: Classification of volcanic features and structures, associations, and global distribution from Magellan data, *J. Geophys. Res.*, *97*, 13,153–13,198, 1992.

Leberl, F. W., *Radargrammetric Image Processing*, Artech House, Norwood, Mass., 1990.

Leberl, F. W., J. K. Thomas, and K. E. Maurice, Initial results from the Magellan stereo experiment, *J. Geophys. Res.*, *97*, 13,675–13,689, 1992.

Lehmann, O., Morphologische theorie der verwitterung von steinschlag wanden, *Vierteljahsschr. Nat. Ges. Zurich*, *87*, 83–126, 1933.

Masursky, H., E. Eliason, P. G. Ford, G. E. McGill, and G. Schubert, Pioneer Venus radar results: Geology from images and altimetry, *J. Geophys. Res.*, *85*, 8232–8260, 1980.

McGill, G. E., S. J. Steenstrup, C. Barton, and P. G. Ford, Continental rifting and the origin of Beta Regio, *Geophys. Res. Lett.*, *8*, 737–740, 1981.

McGill, G. E., J. L. Warner, M. C. Malin, R. E. Arvidson, E. Eliason, S. Nozette, and R. E. Reasenberg, Topography, surface properties and tectonic evolution, in *Venus*, edited by D. M. Hunten et al., pp. 69–130, Univ. of Ariz. Press, Tucson, 1983.

Moore, R. K., Imaging radar systems, in *Manual of Remote Sensing*, edited by R. N. Colwell, pp. 429–474, Am. Soc. of Photogramm. and Remote Sens., Bethesda, Md., 1983.

Pettengill, G. H., P. G. Ford, W. T. K. Johnson, K. Raney, and L. A. Soderblom, Magellan: Radar performance and data products, *Science*, *252*, 260–265, 1991.

Plescia, J. B., and M. P. Golombek, Origin of planetary wrinkle ridges based on the study of terrestrial analogs, *Geol. Soc. Am. Bull.*, *97*, 1289–1299, 1986.

Price, M., and J. Suppe, Mean age of rifting and volcanism on Venus deduced from impact crater densities, *Nature*, *372*, 756–759, 1994.

Sabins, F. F., *Remote Sensing Principles and Interpretation*, 449 pp., W. H. Freeman, New York, 1987.

Sanders, R. S., R. E. Arvidson, J. W. Head, G. G. Schaber, E. R. Stofan, and S. C. Solomon, An overview of Venus geology, *Science*, *252*, 249–252, 1991.

Sanders, R. S., et al., Magellan mission summary, *J. Geophys. Res.*, *97*, 13,067–13,090, 1992.

Schaber, G. G., Venus: Limited extension and volcanism along zones of lithospheric weakness, *Geophys. Res. Lett.*, *9*, 499–502, 1982.

Selby, M. J., *Hillslope Materials and Processes*, 451 pp., Oxford Univ. Press, New York, Oxford, 1993.

Senske, D. A., G. G. Schaber, and E. R. Stofan, Regional topograhic rises on Venus: Geology of western Eistla Regio and comparison to Beta Regio and Alta Regio, *J. Geophys. Res.*, *97*, 13,395–13,420, 1992.

Solomon, S. C., et al., Venus tectonics: An overview of Magellan observations, *J. Geophys. Res.*, *97*, 13,199–13,255, 1992.

Squyres, S. W., D. G. Jankowski, M. Simons, S. C. Solomon, B. H. Hager, and G. E. McGill, Plains tectonism on Venus: The deformation belts of Lavinia Planitia, *J. Geophys. Res.*, *97*, 13,579–13,599, 1992.

Stofan, E. R, J. R. Head, D. B. Campbell, S. H. Zisk, A. F. Bogomolov, O. N. Rzhiga, A. T. Basilevsky, and N. Armand, Venus rift zones: Geology of Beta Regio and Devana Chasma, *Geol. Soc. Am. Bull.*, *101*, 143–156, 1989.

Suppe, J., Geometry and kinematics of fault-bend folding, *Am. J. Sci.*, *283*, 684–721, 1983.

Suppe, J., *Principles of Structural Geology*, 537 pp., Prentice-Hall, Englewood Cliffs, N. J., 1985.

Suppe, J., and C. Connors, Critical taper wedge mechanics of fold-and-thrust belts on Venus: Initial results from Magellan, *J. Geophys. Res.*, *97*, 13,545–13,561, 1992.

Surkov, Y. A., L. P. Moskalyeva, O. P. Scheglov, V. P. Kharyukova, O. S. Manvelyan, V. S. Kirichenko, and A. D. Dudin, Determinations of the elemental composition of rocks on Venus by Venera 13 and Venera 14 (preliminary results), *Proc. Lunar Planet. Sci. Conf. Proc. 13th*, Part 2, *J. Geophys. Res.*, *88*, suppl., A481–A493, 1983.

Terzaghi, K., Stability of steep slopes on hard unweathered rock, *Geotechnique*, *12*, 251–270, 1962.

Tukey, J. W., *Exploratory Data Analysis*, 688 pp., Addison-Wesley, Reading, Mass., 1976.

Walsh, J. J., and J. Watterson, Dips of normal faults in British coal measures and other sedimentary sequences, *J. Geol. Soc. London.*, *145*, 859–873, 1988.

Watters, T. R., Wrinkle ridge assemblages on the terrestrial planets, *J. Geophys. Res.*, *93*, 10,236–10,254, 1988.

Withjack, M. O., Q. T. Islam, and P. R. La Pointe, Normal faults and their hanging-wall deformation: An experimental study, *Am. Assoc. Pet. Geol. Bull.*, *79*(1), 1–18, 1995.

Xiao, H., and J. Suppe, Origin of rollover, *Geol. Soc. Am. Abstr. Programs*, *20*, A109, 1988.

Xiao, H., and J. Suppe, Origin of rollover, *Am. Assoc. Pet. Geol. Bull.*, *76*, 509–529, 1992.

Xiao, H., F. A. Dahlen, and J. Suppe, Mechanics of extensional wedges, *J. Geophys. Res.*, *96*, 10,301–10,318, 1991.

C. Connors, Department of Geology, Washington and Lee University, Lexington, VA 24450. (connorsc@wlu.edu)

J. Suppe, Department of Geological and Geophysical Sciences, Princeton University, Princeton, NJ 08540.

(Received March 27, 2000; revised September 15, 2000; accepted October 13, 2000.)